



## SO<sub>x</sub> uptake and release properties of TiO<sub>2</sub>/Al<sub>2</sub>O<sub>3</sub> and BaO/TiO<sub>2</sub>/Al<sub>2</sub>O<sub>3</sub> mixed oxide systems as NO<sub>x</sub> storage materials

Göksu S. Şentürk<sup>a</sup>, Evgeny I. Vovk<sup>a,b</sup>, Vladimir I. Zaikovskii<sup>b</sup>, Zafer Say<sup>a</sup>, Aslı M. Soylu<sup>a</sup>, Valerii I. Bukhtiyarov<sup>b</sup>, Emrah Ozensoy<sup>a,\*</sup>

<sup>a</sup> Chemistry Department, Bilkent University, 06800 Bilkent, Ankara, Turkey

<sup>b</sup> Borekov Institute of Catalysis, 630090 Novosibirsk, Russian Federation

### ARTICLE INFO

#### Article history:

Received 15 September 2011

Received in revised form

23 November 2011

Accepted 1 December 2011

Available online 30 December 2011

#### Keywords:

Al<sub>2</sub>O<sub>3</sub>

BaO

TiO<sub>2</sub>

Anatase

Sulfur poisoning

DeNO<sub>x</sub>

NO<sub>x</sub>

SO<sub>x</sub>

Sulfation

NSR

LNT

HDS

Claus Process

### ABSTRACT

Titania was used as a promoter to obtain novel materials in the form of TiO<sub>2</sub>/Al<sub>2</sub>O<sub>3</sub> (Ti/Al) and BaO/TiO<sub>2</sub>/Al<sub>2</sub>O<sub>3</sub> (Ba/Ti/Al, containing 8 wt% or 20 wt% BaO) that are relevant to NO<sub>x</sub> storage reduction (NSR) catalysis. Two different protocols (P1, P2) were utilized in the synthesis. Ti/Al(P1) manifests itself as crystallites of TiO<sub>2</sub> on γ-Al<sub>2</sub>O<sub>3</sub>, while Ti/Al(P2) reveals an amorphous Al<sub>x</sub>Ti<sub>y</sub>O<sub>z</sub> mixed oxide. The structures of the synthesized materials were investigated via TEM, EDX, BET analysis and XPS while the catalytic functionality/performance of these support materials upon SO<sub>x</sub> and subsequent NO<sub>x</sub> adsorption were investigated with TPD and in situ FTIR spectroscopy. Ti/Al(P1, P2) revealed a high affinity towards SO<sub>x</sub>. Overall thermal stabilities of the adsorbed SO<sub>x</sub> species and the total SO<sub>x</sub> uptake of the Ba-free samples increase in the following order: TiO<sub>2</sub>(anatase) ≪ γ-Al<sub>2</sub>O<sub>3</sub> < Ti/Al(P1) < Ti/Al(P2). The superior SO<sub>x</sub> uptake of Ti/Al(P1, P2) support materials can be tentatively attributed to the increasing specific surface area upon TiO<sub>2</sub> promotion and/or the changes in the surface acidity. Promotion of BaO/Al<sub>2</sub>O<sub>3</sub> with TiO<sub>2</sub> leads to the attenuation of the SO<sub>x</sub> uptake and a significant decrease in the thermal stability of the adsorbed SO<sub>x</sub> species. The relative SO<sub>x</sub> adsorption capacities of the investigated materials can be ranked as follows: 8Ba/Ti/Al(P1) < 8Ba/Ti/Al(P2) < 8Ba/Al ~ 20Ba/Ti/Al(P1) < 20Ba/Al < 20Ba/Ti/Al(P2).

© 2011 Elsevier B.V. All rights reserved.

## 1. Introduction

Controlling the surface chemistry of mixed-oxide surfaces is of vital importance to design novel catalytic materials with unprecedented functionalities. Sulfur poisoning on metal oxide surfaces is one of the frequently observed surface deactivation phenomena in heterogeneous catalysis. Accumulation of SO<sub>x</sub> species on metal oxide surfaces have been very commonly studied in the literature in relevance to three-way catalysis (TWC), selective catalytic reduction (SCR), NO<sub>x</sub> storage reduction (NSR), hydrodesulfurization (HDS) and other catalytic processes, where Al<sub>2</sub>O<sub>3</sub> is utilized as the main support material [1–7]. Two major deactivation phenomena are often reported for the NSR catalysts. The first route involves thermal degradation of the structural integrity of the catalyst material due to solid state reactions between the catalyst components

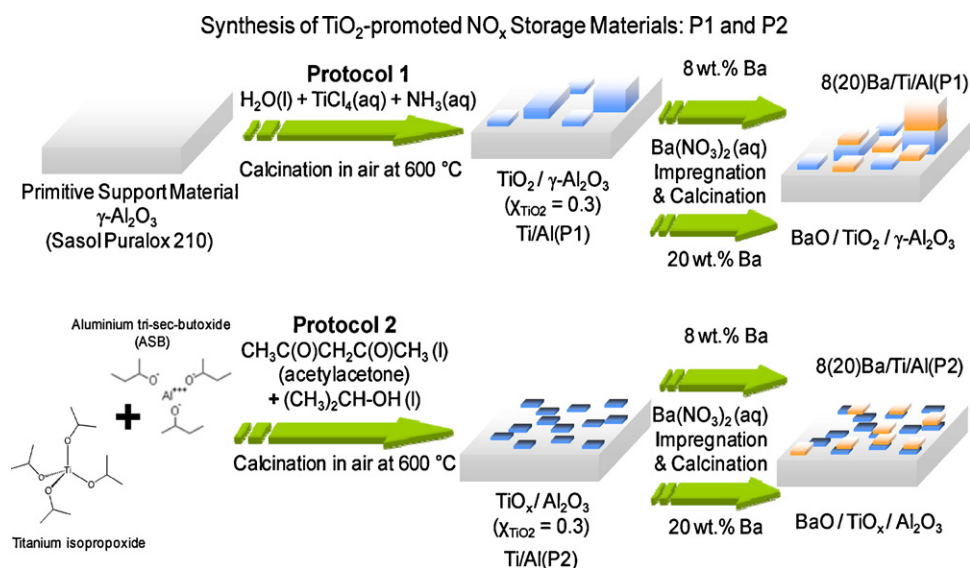
and sintering while the second route is associated with the sulfur poisoning [8,9]. The latter deactivation phenomenon is particularly a challenging problem. In NSR applications, NO<sub>x</sub>(g) and SO<sub>x</sub>(g) adsorbates, compete for the same basic adsorption sites on oxide surfaces. Consequently, maximization of the NO<sub>x</sub> storage capacity (NSC) while minimizing the irreversible SO<sub>x</sub> uptake of the NO<sub>x</sub> storage sites implies careful optimization of the surface properties of the catalytic support materials such as the surface composition, acidity, morphology and specific surface area (SSA).

Sulfur poisoning of NSR catalysts typically leads to the formation of alkaline earth/precious metal sulfates, sulfites or sulfides [8]. For a large number of oxide substrates, the stability of some of the common adsorbates increases in the following order: NO<sub>2</sub><sup>-</sup> ~ CO<sub>3</sub><sup>2-</sup> < NO<sub>3</sub><sup>-</sup> < SO<sub>4</sub><sup>2-</sup> [10–15]. Thus, sulfur effectively blocks the catalytic sites for NO<sub>x</sub> storage and gradually reduces the overall NO<sub>x</sub> storage capacity of the NSR catalysts [16].

Efforts towards improving the catalytic tolerance against sulfur poisoning and designing highly active and stable novel catalysts are vital for the globalization of the NSR technology [14,15,17–20].

\* Corresponding author.

E-mail address: [ozensoy@fen.bilkent.edu.tr](mailto:ozensoy@fen.bilkent.edu.tr) (E. Ozensoy).



**Scheme 1.** Synthesis of TiO<sub>2</sub>-promoted NO<sub>x</sub> storage materials: P1 and P2.

Misono and Inui [21], Fritz and Pitchon [22] and several others [12,13,23–27] reported detailed studies on the improvement and the durability enhancement of NSR catalysts. The commercial catalysts are also successfully used in limited markets such as Japan where the sulfur content of the diesel fuel is relatively low (below 10 ppm) [28]. According to Yamazaki et al., Fe was found to decrease the sulfur uptake and promote the decomposition of BaSO<sub>4</sub> [29]. Fanson et al. observed that Fe facilitated the formation of a bulk nitrate species which were suggested to be resilient against sulfur poisoning [30]. Kayhan et al. reported that the initial NO<sub>x</sub> uptake mechanism and the ratio between the surface and bulk BaO sites were significantly influenced by Fe loading [20].

TiO<sub>2</sub> containing support materials were also reported to suppress the sulfur poisoning [31,32]. This effect was associated with the surface acidity of TiO<sub>2</sub>, inhibiting the adsorption of acidic SO<sub>x</sub> species [33]. Decomposition temperature of the sulfates on pure TiO<sub>2</sub> is known to be lower than that of  $\gamma$ -Al<sub>2</sub>O<sub>3</sub> [34,35]. Furthermore, active sites on the sulfated TiO<sub>2</sub> surface can also be readily regenerated under reaction conditions [36]. Recently, it was also reported that TiO<sub>2</sub> sites on the support surface can function as efficient anchoring sites for BaO, which may be exploited to enhance the surface dispersion of BaO domains and fine-tune the surface morphology [37].

In order to circumvent some of the unfavorable properties of pure TiO<sub>2</sub> such as the limited thermal stability, low surface area, and poor mechanical properties, its combination with secondary oxides are utilized to design novel support materials with enhanced properties. Along these lines,  $\gamma$ -Al<sub>2</sub>O<sub>3</sub> [14,19,32,36,38–42] and/or ZrO<sub>2</sub> [43–45] are promising choices for the secondary oxides that can be used in combination with TiO<sub>2</sub>. It was reported that if sulfur-poisoned Ba/Pt/Al<sub>2</sub>O<sub>3</sub> catalyst was blended with non sulfur-poisoned Pt/TiO<sub>2</sub> catalyst, sulfur desorption from the Ba/Pt/Al<sub>2</sub>O<sub>3</sub> catalyst under rich conditions is improved [14]. Furthermore, it was suggested that the interface between Al<sub>2</sub>O<sub>3</sub> and TiO<sub>2</sub> plays an important role in the sulfate decomposition and the desorption processes [32]. Matsumoto and co-workers [14,46] reported that a combination of TiO<sub>2</sub> and lithium-doped  $\gamma$ -Al<sub>2</sub>O<sub>3</sub> presents an optimum surface acidity towards sulfur poisoning. The macroscopic geometrical structure of the catalytic monolith was also found to be effective in limiting the size of the sulfate particles and controlling the sulfate decomposition/desorption temperature [47,48]. It was shown that sulfate decomposition is facilitated on

the smaller sulfate domains. There also exist a number of surface science studies on planar model NSR catalysts [49–53] focusing on the structure and the operational principles of NSR systems at the molecular level. Despite the established sulfur resisting effect of TiO<sub>2</sub> as an additive in the composition of the Pt/Ba/ $\gamma$ -Al<sub>2</sub>O<sub>3</sub> catalysts, a number of crucial aspects regarding the influence of TiO<sub>2</sub> on the interaction between the NO<sub>x</sub> storage component and the support material have not yet been elucidated.

Thus, in the current work, we focus our attention on the interaction of SO<sub>x</sub> with the TiO<sub>2</sub>/Al<sub>2</sub>O<sub>3</sub> and BaO/TiO<sub>2</sub>/Al<sub>2</sub>O<sub>3</sub> surfaces as well as the influence of TiO<sub>2</sub> domains on the NO<sub>x</sub> uptake after deactivation by SO<sub>2</sub>(g) + O<sub>2</sub>(g).

## 2. Experimental

TiO<sub>2</sub>/Al<sub>2</sub>O<sub>3</sub> binary oxide support materials (which will be hereafter referred as Ti/Al in the text) were prepared via two different synthetic protocols P1 [23,37] and P2 [37] which were described in detail in our former reports. These synthetic protocols were schematically described in Scheme 1. Briefly, in the first synthetic protocol (P1),  $\gamma$ -Al<sub>2</sub>O<sub>3</sub> (PURALOX, 200 m<sup>2</sup>/g, SASOL GmbH, Germany) and TiCl<sub>4</sub> (Fluka, titanium(IV) chloride solution ~0.1 M in 20% hydrochloric acid) were used as starting materials. TiCl<sub>4</sub> was diluted in cooled deionized water under continuous stirring at a temperature below 333 K. Then,  $\gamma$ -Al<sub>2</sub>O<sub>3</sub> powder was slowly added to the prepared solution. Next, 30 vol% NH<sub>3</sub> was slowly added to the solution until pH  $\geq$  9.0 was achieved and a gel was formed. This white gel was aged for 24 h under ambient conditions, filtered, washed with distilled water, and calcined at 873 K for 2 h in air. In the second synthetic protocol (P2), the binary Ti/Al oxide support material was synthesized by a sol gel method. In this synthetic protocol (P2), titanium and aluminum alkoxides were used as precursors. First, aluminum-tri-sec-butoxide (97%, Sigma-Aldrich) was dissolved in the mixture of propan-2-ol (99.5%, Sigma-Aldrich) and acetylacetonate (99.3%, Fluka). Then, titanium(IV) isopropoxide (97%, Sigma-Aldrich) was added to the solution at room temperature. Next, 0.5 M HNO<sub>3</sub> was gradually added to the solution in order to initiate the gel formation. The resulting gel was aged for 10 days under ambient conditions, ground, and baked at 873 K for 2 h in air. The mole fraction of TiO<sub>2</sub> (i.e.  $\chi_{\text{TiO}_2} = n_{\text{TiO}_2} / (n_{\text{TiO}_2} + n_{\text{Al}_2\text{O}_3})$ ) in the TiO<sub>2</sub>/Al<sub>2</sub>O<sub>3</sub> binary mixture was equal to 0.3 (based on the amounts of Ti and Al

precursors used in the synthesis) in both of the synthetic protocols. BaO/TiO<sub>2</sub>/γ-Al<sub>2</sub>O<sub>3</sub> (which will be hereafter referred as Ba/Ti/Al) samples with different Ba loadings (8 and 20 wt% BaO) were synthesized by conventional incipient wetness impregnation of the Ti/Al binary oxide support materials with Ba(NO<sub>3</sub>)<sub>2</sub>. In the current text, samples with 8 and 20 wt% BaO loading will be denoted as 8Ba/Ti/Al(P1, P2) and 20Ba/Ti/Al(P1, P2), respectively. For a comprehensive discussion of the structural characterization of the synthesized materials via SEM, EDX, BET, Raman spectroscopy and XRD, the analysis of the surface acidity of the Ti/Al(P1) and 8/20Ba/Ti/Al(P1) samples via pyridine adsorption, as well as NO<sub>x</sub> adsorption/release properties via FTIR and TPD, reader is referred to our previously published work [23,37] which will also be used frequently in the discussion of the current results. γ-Al<sub>2</sub>O<sub>3</sub> (Puralox, 200 m<sup>2</sup>/g, SASOL GmbH, Germany) used in (P1) synthetic protocol was also utilized as a reference material in some experiments.

TEM images were obtained with a resolution of 0.14 nm on a JEM-2010 (200 keV) microscope equipped with an EDX spectrometer with a Si (Li) detector having an energy resolution of 130 eV. The analyzed area in a typical EDX measurement was about 10 × 10 nm<sup>2</sup>. The samples for the TEM analysis were prepared by dispersing the powders in an ultrasonic ethanol bath and subsequent deposition of the suspension upon a “holey” carbon film supported on a copper TEM grid. XPS data were recorded using a SPECS spectrometer with a PHOIBOS-100 hemispherical energy analyzer and a monochromatic AlK<sub>α</sub> X-ray irradiation ( $h\nu = 1486.74$  eV, 200 W). FTIR spectroscopic measurements were carried out in transmission mode in a batch-type catalytic reactor [20] coupled to an FTIR spectrometer (Bruker Tensor 27) and a quadrupole mass spectrometer (QMS, Stanford Research Systems, RGA 200) used for TPD experiments. All FTIR spectra were acquired at 323 K. In the TPD experiments, a linear temperature ramp with a heating rate of 12 K/min was utilized to heat the sample within 323–1023 K. The QMS signals with  $m/z$  equal to 18(H<sub>2</sub>O), 28(N<sub>2</sub>/CO), 30(NO), 34(H<sub>2</sub>S), 32(O<sub>2</sub>), 44(N<sub>2</sub>O/CO<sub>2</sub>), 46(NO<sub>2</sub>) and 64(SO<sub>2</sub>) were monitored during the TPD measurements. BET SSA and pore size distribution measurements were performed using a Micromeritics Tristar 3000 surface area and pore size analyzer by low-temperature isothermal adsorption–desorption of N<sub>2</sub>.

The sulfur exposure experiments were performed through four different consecutive steps. In the first spectral acquisition step, the sample was exposed to 0.6 Torr of SO<sub>2</sub>(g)+O<sub>2</sub>(g) mixture (SO<sub>2</sub>:O<sub>2</sub> = 1:10) for 1 h at 323 K and the first FTIR spectrum was obtained in the presence of the SO<sub>2</sub>(g)+O<sub>2</sub>(g) mixture over the sample. In the second step, the sample was annealed to 473 K in the presence of the SO<sub>2</sub>(g)+O<sub>2</sub>(g), and after cooling to 323 K, the second FTIR spectrum was acquired. In the third step, before the spectrum acquisition, the sample was annealed to 673 K (in the presence of SO<sub>2</sub>(g)+O<sub>2</sub>(g)), then cooled to 323 K and successively evacuated at 323 K for 20 min ( $P_{\text{reactor}} < 1 \times 10^{-4}$  Torr). In the fourth step, the sample was flashed to 673 K in vacuum and after cooling the sample to 323 K, a FTIR spectrum was obtained. For NO<sub>2</sub> adsorption experiments, the fresh samples were pre-poisoned by an exposure of 0.6 Torr of SO<sub>2</sub>(g)+O<sub>2</sub>(g) (SO<sub>2</sub>:O<sub>2</sub> = 1:10) mixture at 323 K and were further heated in the gas mixture at 473 K for 30 min. After having pumped out the reactor, poisoned sample was exposed to 8 Torr of NO<sub>2</sub>(g) at 323 K for 20 min in order to saturate the surface with NO<sub>x</sub>. This is followed by the evacuation and FTIR spectra acquisition at 323 K.

### 3. Results and discussion

#### 3.1. TEM characterization of Ti/Al materials

Fig. 1 represents the TEM micrographs of the Ti/Al(P1, P2) samples showing the morphology of the synthesized support materials.

EDX analysis of area 1 given in Fig. 1a, which is abundant in darker domains, reveals the presence of TiO<sub>2</sub> and Al<sub>2</sub>O<sub>3</sub> containing species with a Ti:Al atomic ratio equal to 70:30. EDX analysis of the bright domains such as area 2 in Fig. 1a, demonstrated that these areas exclusively contain Al<sub>2</sub>O<sub>3</sub>. However, the Fourier analysis of area 2 in Fig. 1a did not reveal well-defined spots, most likely due to the small particle sizes and the defective nature of these alumina crystallites. The image in Fig. 1b shows a high-resolution TEM (HRTEM) micrograph of such a bright domain.

It is visible in Fig. 1a that the darker domains contain aggregates with sizes of about 10 nm. Fig. 1c shows a HRTEM image of one of these darker domains. Interplanar spacing measured on HRTEM micrographs of these darker domains are in very good agreement with the anatase phase of TiO<sub>2</sub>. Fast Fourier Transform (FFT) picture obtained from this image is also shown as an inset in Fig. 1c and is in good agreement with the reflexes of anatase phase (file no. 21-1272 in PDF-2 Database, JCPDS-ICDD).

Fig. 1d–f shows TEM images of the Ti/Al(P2) sample. It is clearly visible in these images that this sample displays a rather homogeneous morphology exhibiting a uniform sponge-like fine structure which is due to the mesoporous character of the mixed Ti<sub>x</sub>Al<sub>y</sub>O<sub>z</sub> oxide phase that is abundant in TiO<sub>x</sub>/AlO<sub>x</sub> interfaces. Area 1 given in Fig. 1e highlights a characteristic region where this rather homogenous and porous structure is apparent. Ti:Al elemental ratio obtained from the EDX spectrum of area 1 in Fig. 1d is close to 15:85 which is in very good agreement with the nominal composition expected from the relative concentrations of Ti and Al precursors used in the material synthesis (20:80). On the other hand, EDX elemental analysis of a less characteristic (minority) region in Fig. 1d (labeled as area 2) reveals the presence of almost exclusively Al<sub>2</sub>O<sub>3</sub> particles. The TEM image given in Fig. 1e and HRTEM image given in Fig. 1f show the characteristic sponge-like structure of Ti/Al(P2). FFT image of the TEM image given in Fig. 1f is also presented as an inset. Fuzzy character of the FFT image is in agreement with the amorphous character of the Ti<sub>x</sub>Al<sub>y</sub>O<sub>z</sub> oxide phase with small and disordered AlO<sub>x</sub> and TiO<sub>x</sub> domains. However, the steep intensity changes near 0.45 nm from the center shows that disordered structure is probably due to the alumina spinel structure (this distance can be associated with d-spacing between (1 1 1) close packed oxygen planes in the lattice of γ-Al<sub>2</sub>O<sub>3</sub> (file no. 29-0063 in PDF-2 Database, JCPDS-ICDD). FFT filtered picture (Fig. 1g) supports the lack of an ordered crystalline structure. These observations indicate that the Ti/Al(P2) structure is mostly composed of a Ti<sub>x</sub>Al<sub>y</sub>O<sub>z</sub> mixed oxide exhibiting a large concentration of TiO<sub>x</sub>/AlO<sub>x</sub> interfacial sites, while the Ti/Al(P1) reveals an inhomogeneous distribution of larger Al<sub>2</sub>O<sub>3</sub> and TiO<sub>2</sub> agglomerates with a relatively smaller concentration of such interface sites.

#### 3.2. Pore size distribution

BET SSA analysis demonstrates that Ti/Al(P1) and (P2) samples have surface area values of 167.0 and 393.2 m<sup>2</sup>/g, respectively [37]. SSA values of Ti/Al(P1, P2) support materials as well as 8(20)Ba/Ti/Al(P1, P2) materials after thermal treatments within 623–1023 K can be found in one of our former reports [37]. The pore size distributions of these support materials monitored during N<sub>2</sub> desorption are presented in Fig. 2. The Ti/Al(P1) sample shows a relatively broad peak with an average pore size about 80 Å which is probably due to the convolution of the pore size distributions of the discrete TiO<sub>2</sub> and Al<sub>2</sub>O<sub>3</sub> domains, while Ti/Al(P2) sample demonstrates a relatively narrow distribution with an average pore size of 30 Å, corresponding to the Ti<sub>x</sub>Al<sub>y</sub>O<sub>z</sub> mixed oxide network. As can be seen in Fig. 2, the pore size analysis is consistent with the dissimilar surface structures of the Ti/Al(P1) and Ti/Al(P2) support materials.

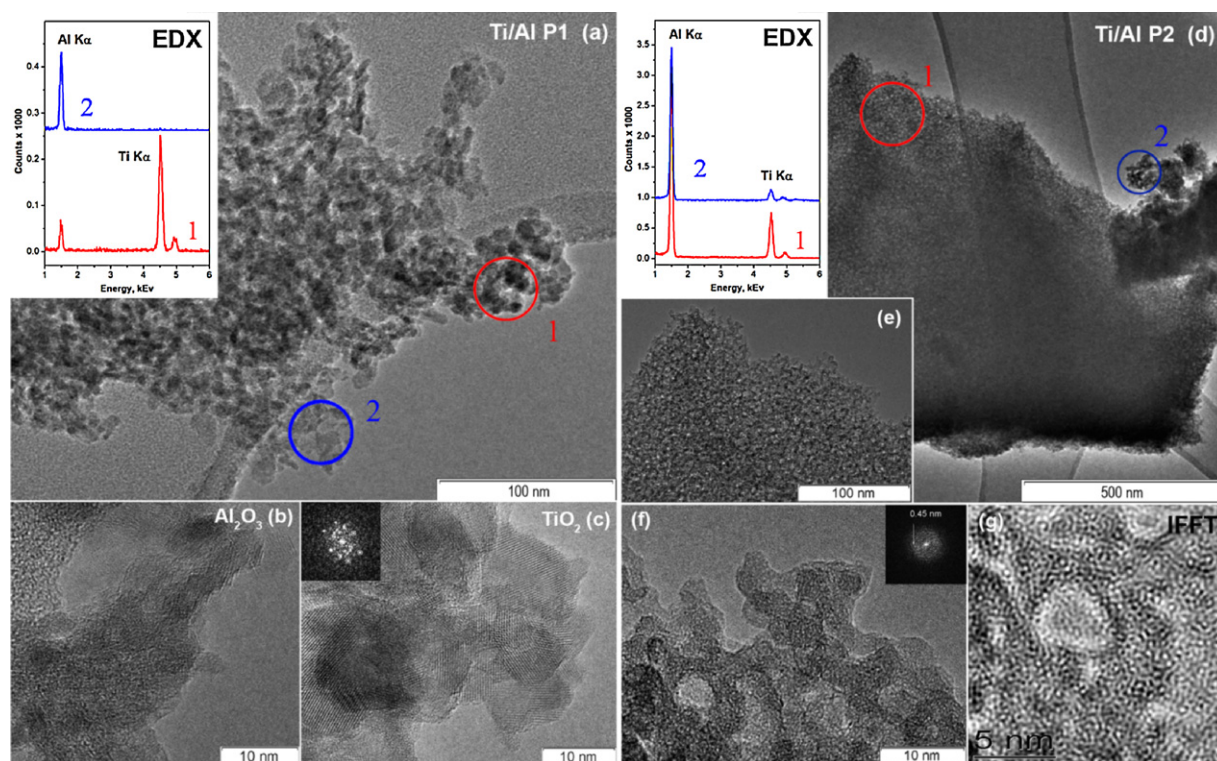


**Fig. 1.** (a–c) TEM images of Ti/Al(P1), region 1: TiO<sub>2</sub>-rich domains, region 2:  $\gamma$ -Al<sub>2</sub>O<sub>3</sub>-rich domains, and (d–g) Ti/Al(P2), region 1: sponge-like structure of the TiO<sub>x</sub>–AlO<sub>x</sub> mixed oxide, region 2: (dark) Al<sub>2</sub>O<sub>3</sub> domains. EDX spectra obtained from selected regions are also given as insets.

### 3.3. SO<sub>x</sub> interaction with Ti/Al and Ba/Ti/Al materials: FTIR

It should be noted that there is not a clear consensus on the vibrational spectroscopic assignments of the SO<sub>x</sub> species on metal oxides (particularly on Al<sub>2</sub>O<sub>3</sub>) due to the heavily convoluted nature of the FTIR signals of the adsorbed SO<sub>x</sub> species. Assignments of the FTIR signals for various SO<sub>x</sub> species discussed in the literature are summarized in Table 1.

We performed FTIR investigations of SO<sub>2</sub>(g) adsorption on  $\gamma$ -Al<sub>2</sub>O<sub>3</sub>. The results (data not shown) are in agreement with the former investigations, revealing the formation of surface sulfites (SO<sub>3</sub><sup>2-</sup>) (note that bulk Al<sub>2</sub>(SO<sub>3</sub>)<sub>3</sub> does not exist [60]), without any additional oxidation to sulfates.

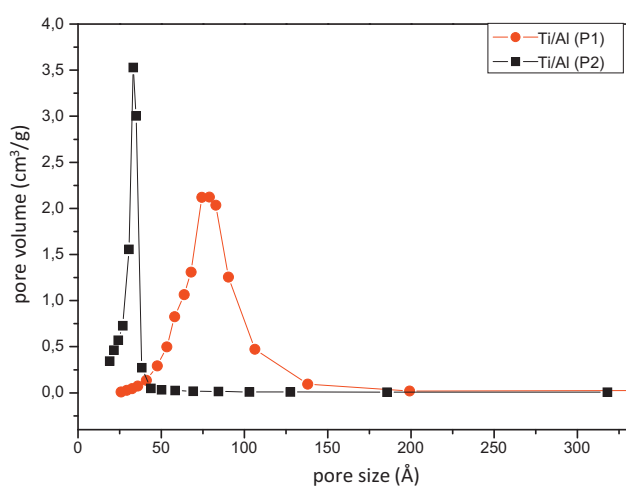


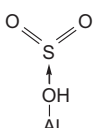
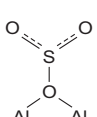
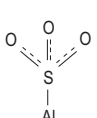
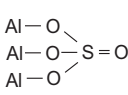
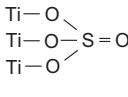
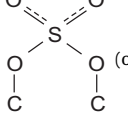
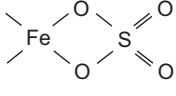
**Fig. 2.** Pore size distribution plots for Ti/Al(P1) and Ti/Al(P2) support materials.

The adsorption of SO<sub>2</sub>(g) + O<sub>2</sub>(g) on the  $\gamma$ -Al<sub>2</sub>O<sub>3</sub> surface at 323 K (Fig. 3a, spectrum i) reveals a major broad band at 1073 cm<sup>-1</sup> as well as weaker and poorly defined additional features around 1350, 1250, 1180 and 1005 cm<sup>-1</sup>. The presence of SO<sub>3</sub><sup>2-</sup> species are apparent due to the intense characteristic sulfite feature at c.a. 1073 cm<sup>-1</sup> ( $\nu_3$ ) and the shoulders at 1049 cm<sup>-1</sup> ( $\nu_3$ ) as well as 1005 cm<sup>-1</sup> ( $\nu_1$ ) [58–60]. Minor features at 1350 ( $\nu_3$ ) and 1180 cm<sup>-1</sup> ( $\nu_1$ ) can be attributed to chemisorbed SO<sub>2</sub> on a basic (O<sup>2-</sup>) surface sites [59,60] while the feature located at 1250 cm<sup>-1</sup> can be associated with the SO<sub>2</sub> adsorbed on Al<sup>3+</sup> Lewis acid sites and/or bidentate sulfates [59]. A very minor contribution from the SO<sub>2</sub>(g) species may also be present at 1130 ( $\nu_3$ ), 1150 ( $\nu_1$ ) and 2499 cm<sup>-1</sup> ( $\nu_1 + \nu_3$ , not shown) [60].

As the adsorption temperature increases to 473 K (Fig. 3a, spectrum ii) the 1368, 1102 signals become more visible which correspond to the  $\nu_3$  and  $\nu_1$  modes of surface sulfates on Al<sub>2</sub>O<sub>3</sub>, [60], respectively. Furthermore, the shoulder located at 1170 cm<sup>-1</sup> which can be associated with bulk Al<sub>2</sub>(SO<sub>4</sub>)<sub>3</sub> [56] starts to be more discernible. In addition, a relatively minor contribution from sulfate species that are interacting with the surface –OH groups which reveal typical signals at 1290 and 1080 cm<sup>-1</sup> cannot be excluded [58]. Increasing the temperature to 673 K (Fig. 3a, spectra iii and iv) results in the growth of the surface and bulk alumina sulfates in expense of the surface sulfite and chemisorbed SO<sub>2</sub> species.

These results indicate that sulfites are initially formed on the alumina surface during the SO<sub>2</sub> + O<sub>2</sub> adsorption at 323 K while at elevated temperatures (473–673 K), these species are converted into relatively stable surface sulfates (SO<sub>4</sub><sup>2-</sup>/Al<sub>2</sub>O<sub>3</sub>) as well as bulk Al<sub>2</sub>(SO<sub>4</sub>)<sub>3</sub>. The formation of sulfates on alumina surface was considered in numerous former studies [56,57,60,68]. Typically, SO<sub>2</sub> binds to the acidic sites (i.e. coordinately unsaturated aluminum cations, Al<sup>3+</sup>) forming physisorbed SO<sub>2</sub>. The adsorption of SO<sub>2</sub> on the basic adsorption sites is followed by a cleavage of an Al–O bond on the surface (primarily at OH sites or at exposed oxygen atoms,

**Table 1**  
Typical FTIR signals associated with common SO<sub>x</sub> species [7,54–67].

Species	Symmetry	$\nu_1$ (cm <sup>-1</sup> )	$\nu_3$ (cm <sup>-1</sup> )	References
SO <sub>2</sub> (gas)	C <sub>2v</sub>	1151	1362	[54]
SO <sub>3</sub> <sup>2-</sup> (free ion)	C <sub>3v</sub>	961	1010	[54,55]
SO <sub>4</sub> <sup>2-</sup> (free ion)	T <sub>d</sub>		1104	[54]
 (physisorbed)	C <sub>2v</sub>	1135–1150	1300–1370	[7,55–58]
 (chemisorbed)	C <sub>2v</sub>		1255 (type I), 1189 (type II)	[59]
	C <sub>s</sub>	1148–1150	1330–1334	[55,59]
	C <sub>2v</sub>	1140	1320–1326	[55,59,60]
	C <sub>3v</sub>	1050–1065	1135	[56,59]
	C <sub>3v</sub>	1045–1130	1380	[58,61]
	C <sub>3v</sub>	1005,1045	1370	[61]
 (organic sulfates)	C <sub>2v</sub>	1230–1150	1440–1350	[62,63]
				
	C <sub>2v</sub>	~910	960–1000	
	C <sub>2v</sub>	1180, 968	1375, 1025	[64]
(NH <sub>4</sub> ) <sub>2</sub> SO <sub>4</sub>	C <sub>2v</sub>	1090	1390	[65]
BaSO <sub>4</sub> (surface)		1060	1120	[66]
Ce(SO <sub>4</sub> ) <sub>2</sub> (surface)		980	1340–1400	[67]
Al <sub>2</sub> (SO <sub>4</sub> ) <sub>3</sub> (bulk)		1190		[56]
BaSO <sub>4</sub> (bulk)		1155, 1248		[66]
Ce(SO <sub>4</sub> ) <sub>2</sub> (bulk)		1145–1240		[67]

O<sup>2-</sup>) leading to the formation of chemisorbed SO<sub>3</sub><sup>2-</sup>. The oxidation of adsorbed SO<sub>3</sub><sup>2-</sup>/SO<sub>2</sub> in oxygen at relatively high temperatures (673–773 K) leads to the formation of surface sulfate species which are coordinated to the metal cations of the oxide surface through three oxygen atoms [60].

In order to examine the sulfur accumulation on the TiO<sub>2</sub> (anatase) surface, SO<sub>2</sub>+O<sub>2</sub> adsorption experiments were also performed on TiO<sub>2</sub> (Fig. 3b). At 323 K (Fig. 3b, spectrum i)

a complex and a convoluted group of signals were observed within 1150–950 cm<sup>-1</sup> which are likely to be associated with SO<sub>3</sub><sup>2-</sup> and/or HSO<sub>3</sub><sup>-</sup> species [60]. At 473 K, the feature at 1137 cm<sup>-1</sup> starts to grow together with an intense feature at 1350 cm<sup>-1</sup>. In analogy with the similar behavior observed for the Al<sub>2</sub>O<sub>3</sub> surface, these two bands are assigned to weakly adsorbed molecular SO<sub>2</sub> species. This assignment is also consistent with the attenuation of the 1137 cm<sup>-1</sup> signal after evacuation at 673 K (Fig. 3b, spectrum iv).

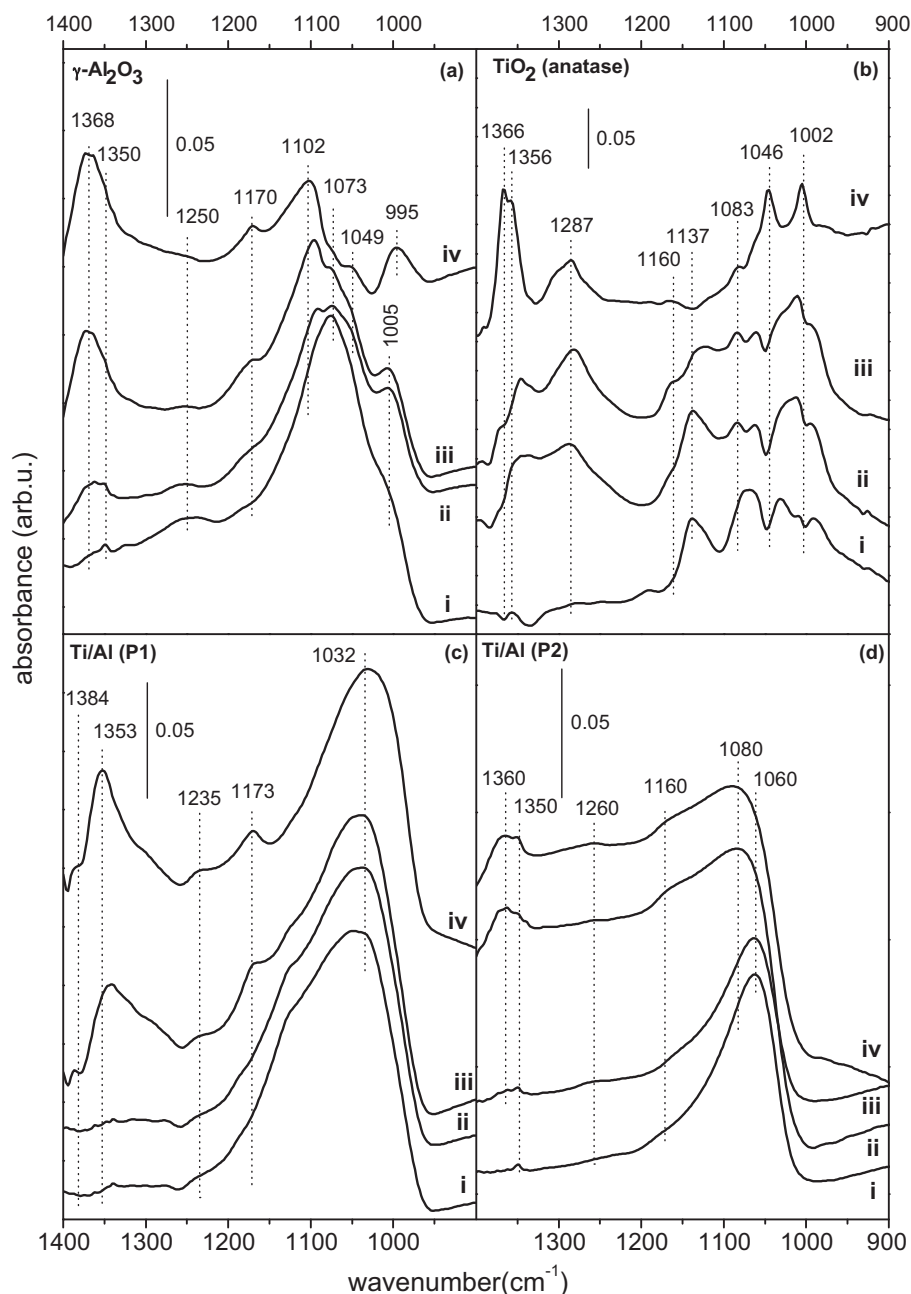


**Fig. 3.** FTIR spectra for 0.6 Torr  $\text{SO}_2(\text{g}) + \text{O}_2(\text{g})$  ( $\text{SO}_2:\text{O}_2 = 1:10$ ) co-adsorption on (a)  $\gamma\text{-Al}_2\text{O}_3$ , (b)  $\text{TiO}_2$  (anatase), (c)  $\text{Ti}/\text{Al}(\text{P1})$ , (d)  $\text{Ti}/\text{Al}(\text{P2})$ . (i) After 1 h exposure to  $\text{SO}_2(\text{g}) + \text{O}_2(\text{g})$  at 323 K (spectrum was obtained in the presence of the gas mixture), (ii) after subsequent flashing of the sample to 473 K in  $\text{SO}_2(\text{g}) + \text{O}_2(\text{g})$  mixture and cooling to 323 K (spectrum was obtained in the presence of the gas mixture), (iii) after subsequent flashing to 673 K in  $\text{SO}_2(\text{g}) + \text{O}_2(\text{g})$  mixture and further evacuation at 323 K ( $P_{\text{reactor}} < 1 \times 10^{-4}$  Torr), (iv) after subsequent flashing the sample to 673 K in vacuum and cooling to 323 K.

Note that it is difficult to follow the fate of the  $1350\text{ cm}^{-1}$  at elevated temperatures since new bands starts to grow in the same spectral region at 673 K. The feature located at  $1287\text{ cm}^{-1}$  together with the  $1083\text{ cm}^{-1}$  feature can be attributed to bidentate sulfates interacting with the adsorbed water at 473–673 K [58] and ortho-chelating bidentate sulfates which reveal vibrational features in a similar range [64,69]. After the evacuation at 673 K, relatively well-resolved features are observed in the FTIR data (Fig. 3b, spectrum iv). Thus the bands at  $1366\text{--}1356$ ,  $1160$ ,  $1046$  and  $1002\text{ cm}^{-1}$  are assigned to surface sulfates on the  $\text{TiO}_2$  surface which are formed after the oxidation of the adsorbed  $\text{SO}_x$  species at 673 K [61,70].

Fig. 3c and d shows the IR spectra of the  $\text{Ti}/\text{Al}(\text{P1})$  and  $\text{Ti}/\text{Al}(\text{P2})$  support materials after treatment in  $\text{SO}_2 + \text{O}_2$  at different temperatures (323–673 K), followed by evacuation. The IR spectra due to

the  $\text{SO}_2 + \text{O}_2$  adsorption on  $\text{Ti}/\text{Al}(\text{P1}, \text{P2})$  at 323 and 473 K (spectra i and ii in Fig. 3c and d) exhibit a strong resemblance where the most prominent feature is the broad IR signal at  $\sim 1050\text{ cm}^{-1}$  corresponding to sulfite species. The main difference between these two spectra is the presence of the shoulder at  $1130\text{ cm}^{-1}$  for the  $\text{Ti}/\text{Al}(\text{P1})$  sample which may be likely due to weakly adsorbed  $\text{SO}_2$  species, similar to the ones that were observed for both pure anatase and  $\gamma$ -alumina surfaces. Increasing the temperature to 673 K in the presence of  $\text{SO}_2 + \text{O}_2$  leads to the formation of additional features associated with surface sulfates at  $1350\text{--}1360$  and  $1160\text{--}1175\text{ cm}^{-1}$  on both  $\text{Ti}/\text{Al}(\text{P1}, \text{P2})$  samples. High temperature  $\text{SO}_2 + \text{O}_2$  exposure also seem to trigger the growth of the convoluted band at  $1230\text{--}1260\text{ cm}^{-1}$  on both samples, which may indicate the formation of bidentate sulfates. The presence of the

1160–1170  $\text{cm}^{-1}$  signal in Fig. 3c and d also suggests the possible formation of bulk  $\text{Al}_2(\text{SO}_4)_3$  species. A general comparison of the line shapes of the FTIR spectra given in Fig. 3c and d reveals that sulfate containing surface domains on the Ti/Al(P1) sample are relatively more ordered and well-crystallized with respect to that of the Ti/Al(P2) sample, which is consistent with the sharper and better resolved sulfate bands visible in Fig. 3c.

Analogous experiments were also performed with Ba containing samples. In these studies, conventional 8(20)Ba/Al benchmark samples that do not contain  $\text{TiO}_2$ , were compared with 8(20)Ba/Ti/Al(P1,P2) samples containing  $\text{TiO}_2$ . After the introduction of a  $\text{SO}_2 + \text{O}_2$  mixture onto the 8Ba/Al and 20Ba/Al samples at 323 K (Fig. 4a and c, spectra i) a major broad band at 1080  $\text{cm}^{-1}$ , which can be attributed to sulfite species, is observed. After subsequent heating at 473 K (in the  $\text{SO}_2 + \text{O}_2$  gas mixture) no substantial changes are observed in the case of the 8Ba/Al sample (Fig. 3a, spectrum ii), while in the case of 20Ba/Al, two different features at 1250 and 1160  $\text{cm}^{-1}$  become apparent. These features can be assigned to bulk  $\text{BaSO}_4$  [66]. Subsequent heating at 673 K in  $\text{SO}_2 + \text{O}_2$  mixture (Fig. 4a, spectrum iii) and in vacuum (Fig. 4a, spectrum iv) leads to the appearance of the bulk  $\text{BaSO}_4$  bands for the 8Ba/Al sample. The additional signal at 1350  $\text{cm}^{-1}$  is associated with surface sulfates on alumina domains. This band is more pronounced for the 8Ba/Al sample, in comparison to the 20Ba/Al surface due to the larger number of exposed alumina sites in the former case as a result of the lower BaO loading.

The sulfation experiments of 8Ba/Ti/Al(P1) and 20Ba/Ti/Al(P1) samples are presented in Fig. 4b and d. After  $\text{SO}_2 + \text{O}_2$  exposure at 323 K, a set of broad and overlapping bands appear within 1100–980  $\text{cm}^{-1}$  indicating the formation of various sulfite species. Interestingly, only insignificantly minor changes are observed for the 8Ba/Ti/Al(P1) sample even after high temperature treatment (Fig. 4b, spectra ii–iv) indicating that the formation of surface aluminum sulfate and bulk  $\text{BaSO}_4$  species is rather suppressed. The changes observed for the 20Ba/Ti/Al(P1) sample are more pronounced (Fig. 4d): bulk  $\text{BaSO}_4$  related features at 1260 and 1160  $\text{cm}^{-1}$  appear after heating at 473 K and these bands become slightly more intense after subsequent heating at 673 K. It is clear that suppression of bulk  $\text{BaSO}_4$  formation by  $\text{TiO}_2$  promotion is effective for the 8Ba/Ti/Al(P1) sample while it is less efficient for 20Ba/Ti/Al(P1) sample. We have reported in our previous studies that  $\text{TiO}_2$  domains function as anchoring sites for BaO sites and limit the surface diffusion of BaO clusters [23,37]. Thus, it is likely that for low BaO loadings, most of the BaO domains on the 8Ba/Ti/Al(P1) sample can effectively bind to  $\text{TiO}_2$  domains, and prevent the sintering of BaO domains. Thus, for low BaO loadings,  $\text{TiO}_2$  domains can efficiently suppress the formation of large BaO clusters where thermally stable bulk  $\text{BaSO}_4$  can form. On the other hand, for higher BaO loadings, as in the case of 20Ba/Ti/Al(P1), a larger fraction of the BaO domains are located on the alumina surface where they can diffuse faster and form larger 3D BaO clusters which can enable the formation of bulk  $\text{BaSO}_4$  as in the case of 20Ba/Al (Fig. 4c). It is worth mentioning that similar experiments were also performed on 8(20)Ba/Ti/Al(P2) samples (data not shown) and a qualitatively similar behavior was observed indicating the significance of the Ba/Ti ratio in the promotional effect of Ti in  $\text{SO}_x$  uptake.

In order to quantitatively compare the amount of  $\text{SO}_x$  stored on the investigated surfaces, XPS analysis of the poisoned samples was performed. Because of the relatively low sensitivity of the XPS technique towards sulfur, poisoning procedure was modified to obtain a better signal to noise ratio and more accurate atomic ratio values. Thus, before the atomic ratio determination by XPS, the samples were poisoned in 10 Torr of  $\text{SO}_x$  ( $\text{SO}_2:\text{O}_2 = 1:10$ ) at 673 K for 30 min. The shape of the FTIR spectra recorded after this poisoning procedure (data not shown) were in very good agreement

with the corresponding spectra presented in Figs. 3 and 4. Binding energy (BE) of S 2p (168–170 eV) XPS signal indicated the presence of mainly sulfates (i.e.  $\text{S}^{6+}$  states) on all samples. It is worth mentioning that although in situ FTIR data given in Fig. 4b suggest the presence of mostly sulfite species on the 8Ba/Ti/Al(P1) sample, XPS data indicates the presence of predominantly sulfate species. This may be associated with the exposure of the 8Ba/Ti/Al(P1) sample to atmosphere before the XPS analysis resulting in the oxidation of sulfites into sulfates. Fig. 5 demonstrates that under identical poisoning conditions, Ti/Al(P1, P2) samples accumulate up to 3–5 times more sulfur than  $\gamma\text{-Al}_2\text{O}_3$ . This behavior might be originating from the larger SSA of the Ti/Al materials in comparison to  $\gamma\text{-Al}_2\text{O}_3$  as well as the decreasing number of total Lewis acid sites in mixed Ti/Al oxides. The less acidic Ti/Al mixed oxide surfaces can demonstrate a higher affinity towards acidic  $\text{SO}_x$ . The acidity of  $\text{TiO}_2\text{-Al}_2\text{O}_3$  mixed oxides as well as  $\gamma\text{-Al}_2\text{O}_3$  has been investigated in previous studies [23,71] by pyridine adsorption. It was suggested that addition of  $\text{TiO}_2$  to  $\text{Al}_2\text{O}_3$  introduces some medium strength Lewis acid sites, [23] however it was demonstrated in another study that the total amount of Lewis acid sites is decreased by 30% for  $\text{TiO}_2\text{-Al}_2\text{O}_3$  in comparison to pure alumina [71].

Analysis of Fig. 5 also reveals that for an identical mass of each material (i.e. 20 mg), 8Ba/Ti/Al(P1, P2) samples accumulate a lesser quantity of sulfur than the 8Ba/Al sample, demonstrating the favorable promotional effect of Ti on limiting sulfur accumulation. Furthermore, 8Ba/Ti/Al(P2) sample seems to store more  $\text{SO}_x$  (per unit sample weight) than the 8Ba/Ti/Al(P1) sample which can be explained by the larger SSA of the former material (185  $\text{cm}^2/\text{g}$  vs. 150  $\text{cm}^2/\text{g}$ , respectively) [37]. However, it is important to mention that the promotion of 8Ba/Al sample with  $\text{TiO}_2$  favorably decreases the total  $\text{SO}_x$  uptake (per unit sample weight) regardless of the preparation method (i.e. P1 or P2) (note that the SSA of the fresh 8Ba/Al sample is 185  $\text{cm}^2/\text{g}$  [20]). This trend is partially reversed when the BaO loading is increased to 20 wt%. Fig. 5 reveals that although 20Ba/Ti/Al(P1) sample (SSA = 79  $\text{cm}^2/\text{g}$  [37]) stores a lesser quantity of  $\text{SO}_x$  (per unit sample weight) than that of 20Ba/Al sample (SSA = 126  $\text{cm}^2/\text{g}$  [20]); 20Ba/Ti/Al(P2) sample (SSA = 173  $\text{cm}^2/\text{g}$  [37]) stores a greater total amount of  $\text{SO}_x$ . These results suggest that for higher BaO loadings, the promotional effect of  $\text{TiO}_2$  is weaker. Besides these SSA trends, this observation may also arise from the fact that not all of the BaO domains are located on the  $\text{TiO}_2$  sites for high BaO loadings and a large fraction of the BaO domains directly interact with the underlying alumina sites as in the case of 20Ba/Al system.

#### 3.4. Influence of $\text{SO}_x$ poisoning on the $\text{NO}_x$ adsorption

$\text{NO}_x$  adsorption on fresh Ti/Al(P1, P2) and fresh 8(20)Ba/Ti/Al(P1, P2) samples via FTIR technique and the corresponding assignments of the observed vibrational bands were thoroughly discussed in one of our recent reports [37] and thus will not be reiterated here. In the light of these previous studies, similar  $\text{NO}_x$  adsorption experiments were also performed on the sulfur-poisoned materials and the results were analyzed.

Fig. 6a compares the  $\text{NO}_x$  uptake characteristics of the fresh and poisoned  $\gamma\text{-Al}_2\text{O}_3$  surface at 323 K. After the saturation of the fresh  $\gamma\text{-Al}_2\text{O}_3$  surface with  $\text{NO}_2(\text{g})$ , vibrational features associated with different types of nitrate species were observed. These nitrate species adsorbed on  $\gamma\text{-Al}_2\text{O}_3$  were in the form of bridged (1258, 1628  $\text{cm}^{-1}$ ), bidentate (1300, 1604  $\text{cm}^{-1}$ ) and monodentate nitrates (1300, 1564  $\text{cm}^{-1}$ ) [37,72]. Additionally, the weak band located at  $\sim 1958 \text{cm}^{-1}$  that was formed after  $\text{NO}_x$  adsorption on the poisoned surface is associated with the adsorbed  $\text{NO}^+$  and/or weakly adsorbed  $\text{N}_2\text{O}_3$  [73]. The poisoning of the  $\gamma\text{-Al}_2\text{O}_3$  surface by  $\text{SO}_2 + \text{O}_2$  decreases the intensities of the nitrate signals, indicating a decline in the  $\text{NO}_x$  uptake of the  $\gamma\text{-Al}_2\text{O}_3$  surface. It is seen

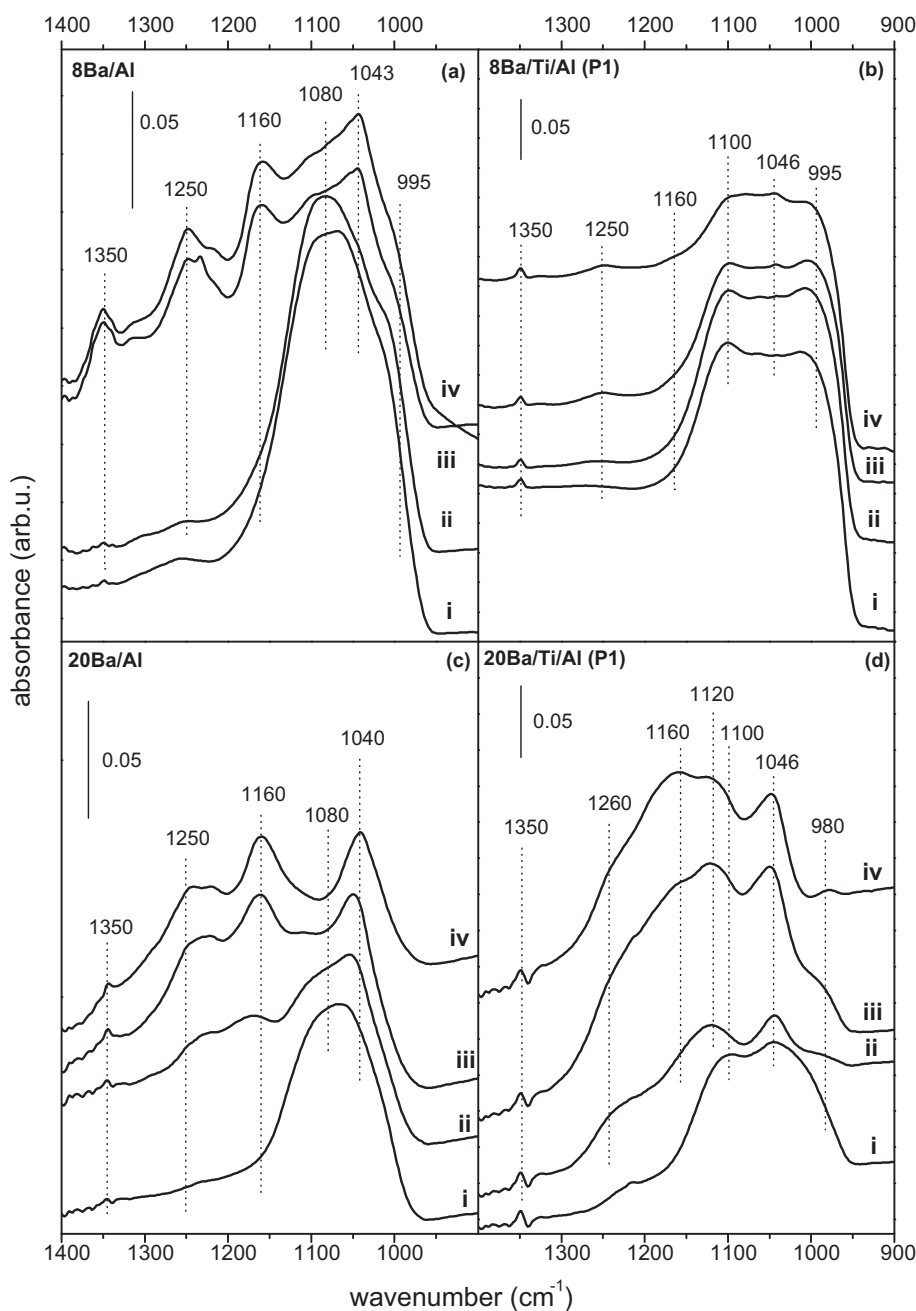


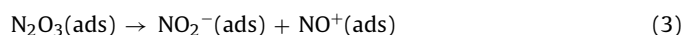
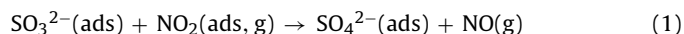
**Fig. 4.** FTIR spectra for 0.6 Torr  $\text{SO}_2(\text{g}) + \text{O}_2(\text{g})$  ( $\text{SO}_2:\text{O}_2 = 1:10$ ) co-adsorption on (a) 8Ba/Al, (b) 8Ba/Ti/Al(P1), (c) 20Ba/Al, (d) 20Ba/Ti/Al(P1). (i) After 1 h exposure to  $\text{SO}_2(\text{g}) + \text{O}_2(\text{g})$  at 323 K (spectrum was obtained in the presence of the gas mixture), (ii) after subsequent flashing of the sample to 473 K in  $\text{SO}_2(\text{g}) + \text{O}_2(\text{g})$  mixture and cooling to 323 K (spectrum was obtained in the presence of the gas mixture), (iii) after subsequent flashing to 673 K in  $\text{SO}_2(\text{g}) + \text{O}_2(\text{g})$  mixture and further evacuation at 323 K ( $P_{\text{reactor}} < 1 \times 10^{-4}$  Torr), (iv) after subsequent flashing the sample to 673 K in vacuum and cooling to 323 K.

in Fig. 6a that  $\text{SO}_x$  poisoning decreases the relative ratio of monodentate and bidentate nitrates ( $1300 \text{ cm}^{-1}$ ) to the bridged nitrates ( $1258 \text{ cm}^{-1}$ ). This observation suggests that sulfate species on the  $\gamma\text{-Al}_2\text{O}_3$  surface suppress the formation of all types of nitrates, particularly the monodentate and bidentate nitrates by occupying the corresponding adsorption sites.

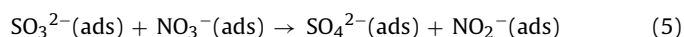
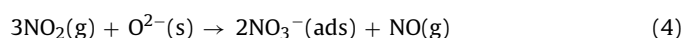
The appearance of the bands at  $1375$  and  $1100 \text{ cm}^{-1}$  in Fig. 6a for the poisoned sample indicates the formation of surface sulfates. Although sulfate formation on the  $\gamma\text{-Al}_2\text{O}_3$  surface in the absence of  $\text{NO}_x$  species (Fig. 3a) requires a relatively high temperature (i.e. 673 K), sulfate formation can readily occur by exposing the alumina surface to  $\text{SO}_2(\text{g}) + \text{O}_2(\text{g})$  at 473 K followed by  $\text{NO}_2(\text{g})$  exposure at 323 K. It is apparent that,  $\text{NO}_x$  species function as efficient oxidizing agents in the oxidation of the  $\text{SO}_2$  and  $\text{SO}_3^{2-}$  to sulfates on the

$\gamma\text{-Al}_2\text{O}_3$  surface. The following reaction pathways can be suggested for the interaction between surface  $\text{SO}_x$  species and the adsorbed  $\text{NO}_x$  species on  $\gamma\text{-Al}_2\text{O}_3$ :

I:



II:



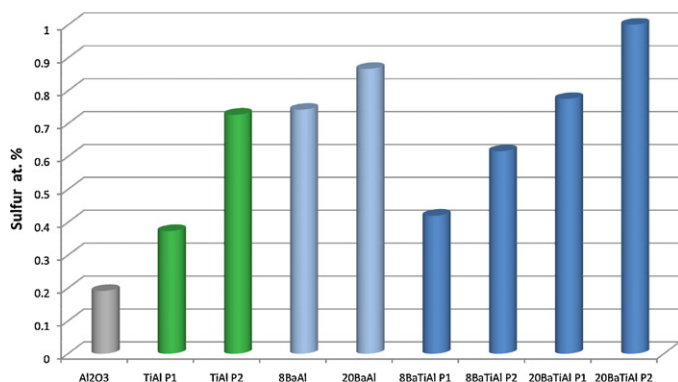
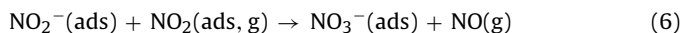


**Fig. 5.** Relative sulfur content (i.e. percentile of sulfur atoms on the surface with respect to all other atoms) of the investigated samples after sulfur poisoning (as described in the text) determined by ex situ XPS analysis.



*Pathway I* suggests that the sulfite species on the  $\gamma\text{-Al}_2\text{O}_3$  surface that are formed in the process of poisoning can be directly oxidized to sulfates with the help of  $\text{NO}_2(\text{g})$  or weakly adsorbed molecular  $\text{NO}_2$ . On the other hand, *pathway II* proposes an alternative route for the sulfate formation, where surface nitrate species facilitate the oxidation of surface sulfites (or weakly adsorbed molecular  $\text{SO}_2$  species). In this latter route, during the sulfate formation, nitrates are consumed at the expense of nitrite and  $\text{NO}$  ( $\text{NO}^+$ ) or  $\text{N}_2\text{O}_3$  generation. The observation of  $1958\text{ cm}^{-1}$  feature in the FTIR spectrum corresponding to the poisoned sample in Fig. 6a, which is not present in the corresponding spectrum for the fresh sample, supports the formation of  $\text{N}_2\text{O}_3/\text{NO}^+$  (reactions (2) and (7)). It is difficult to assess which of these two pathways is favored on the surface under the current experimental conditions. However, by taking into account the facile formation of nitrate species on the  $\gamma\text{-Al}_2\text{O}_3$  surface, it can be argued that *pathway II* may presumably be occurring more readily than *pathway I*.

Fig. 6b, presents analogous poisoning and subsequent  $\text{NO}_x$  uptake experiments conducted on pure  $\text{TiO}_2$  (anatase). The Lewis acid sites on the anatase surface reveal four and five-coordinated  $\text{Ti}^{4+}$  ions (referred as  $\alpha$  and  $\beta$  sites, respectively) where  $\alpha$ -Lewis acid sites (with two oxygen vacancies) favor bidentate ( $1578$  and shoulder at  $\sim 1220\text{ cm}^{-1}$ ) and bridge ( $1627$  and  $1236\text{ cm}^{-1}$ ) nitrate formation while the  $\beta$ -sites ( $\text{Ti}^{4+}$  with one oxygen vacancy) favor the formation of monodentate nitrates (group of features at  $1550\text{--}1500\text{ cm}^{-1}$  and peak at  $1282\text{ cm}^{-1}$ ) [37,74–77]. Similar FTIR signals, though with reduced intensities of all  $\text{NO}_x$  vibrational signals are also observed for the poisoned anatase sample marked in red in Fig. 6b. The poisoned anatase sample also shows some additional bands at  $1359$  and  $1030\text{--}1070\text{ cm}^{-1}$  that are associated with the sulfite and sulfate species.

Similar experiments were also performed on Ti/Al(P1, P2) surfaces as shown in Fig. 6c and d. It is readily seen that the  $\text{NO}_x$  uptake is suppressed by  $\text{SO}_x$  poisoning on both surfaces. It is visible in Fig. 6 that the extent of the nitrate signal suppression is more pronounced for Ti/Al(P1, P2) samples in comparison with pure  $\gamma\text{-Al}_2\text{O}_3$  and  $\text{TiO}_2$ . This result is in agreement with the XPS data given in Fig. 5, indicating a significantly higher affinity of Ti/Al(P1, P2) towards  $\text{SO}_x$  than that of pure  $\gamma\text{-Al}_2\text{O}_3$ . Such a behavior can be explained by an increase in the SSA values and a decrease in the total number of Lewis acid sites upon  $\text{TiO}_2$  promotion. A similar interesting behavior was also reported in the literature for  $\text{TiO}_2\text{-ZrO}_2$  mixed oxide systems. For instance, it is known that pure  $\text{TiO}_2$  (anatase) or pure  $\text{ZrO}_2$  (monoclinic/tetragonal) have very limited  $\text{NO}_x$  storage capacities [78]. On the other hand, when these two different types

of oxides are combined to obtain an amorphous  $\text{TiO}_2\text{-ZrO}_2$  mixed oxide,  $\text{NO}_x$  storage capacity can be improved by more than an order of magnitude, which was attributed to the formation of new Lewis basic sites at the  $\text{TiO}_2\text{-ZrO}_2$  hetero-junctions [78]. In analogy with these observations, Ti/Al(P1, P2) surfaces may also contain new and strong  $\text{SO}_x$  adsorption sites, which are not present on either pure  $\text{TiO}_2$  or  $\gamma\text{-Al}_2\text{O}_3$  surfaces.

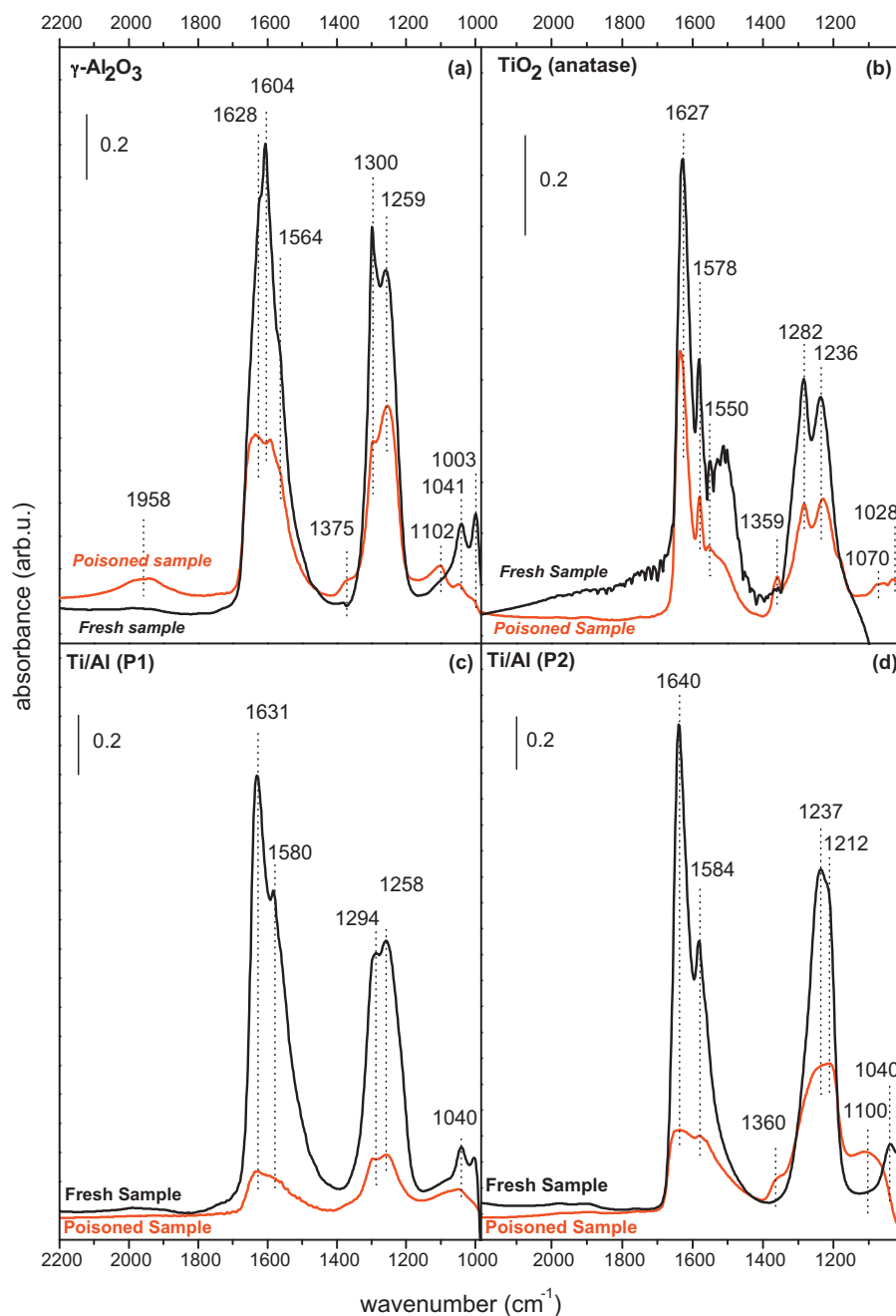
When the relative poisoning of Ti/Al(P1) is compared to that of Ti/Al(P2) (Fig. 6c and d), it is visible that nitrate features are suppressed to a lesser extent on Ti/Al(P2), although the intensities of sulfate features ( $1360$  and  $1100\text{ cm}^{-1}$ ) are stronger on Ti/Al(P2) (Fig. 5d). This observation suggests that the porous and disordered surface morphology of the Ti/Al(P2) sample results in a larger overall  $\text{SO}_x$  uptake, however due to its large surface area (SSA of fresh Ti/Al(P1) and Ti/Al(P2) are  $167$  and  $393\text{ m}^2/\text{g}$ , respectively [37]), Ti/Al(P2) surface still possesses a larger number of  $\text{NO}_x$  binding sites with respect to Ti/Al(P1). On the other hand, such a comparison based solely on IR intensities should be considered with caution, as the IR absorption cross-sections of adsorbed nitrate species with dissimilar adsorption configurations can be significantly different, which may render a direct IR intensity comparison relatively inaccurate.

Fig. 7 compares the  $\text{NO}_x$  adsorption properties of 8(20)Ba/Ti/Al(P1, P2), samples before and after  $\text{SO}_x$  adsorption at  $323\text{ K}$ . The FTIR results corresponding to the adsorption of  $\text{NO}_2$  on the fresh samples were already discussed elsewhere [37]. Briefly, upon  $\text{NO}_2$  adsorption, the fresh sample surfaces are characterized by adsorption bands due to the presence of the bulk (ionic) Ba-nitrates located at  $\sim 1320$ ,  $\sim 1440$  and  $\sim 1480\text{ cm}^{-1}$ , surface (bidentate) Ba-nitrate features located at  $1585$ ,  $1565$ ,  $1300\text{ cm}^{-1}$  and additional nitrate bands at  $1583$  and  $\sim 1630\text{ cm}^{-1}$  that are associated with nitrates adsorbed on the  $\text{TiO}_2$  domains having bidentate and bridged configurations. After  $\text{SO}_x$  poisoning of the samples with  $\text{SO}_2 + \text{O}_2$  at  $473\text{ K}$ , it is clearly visible that the  $\text{NO}_x$  storage capacities decrease significantly. Additionally, the presence of minor bands at  $\sim 1150$  and  $\sim 1245\text{ cm}^{-1}$  implies the existence of sulfate species on all of the samples. Formation of sulfate species on all of the samples after subsequent  $\text{NO}_2$  adsorption at  $323\text{ K}$  demonstrates the efficient oxidizing capability of  $\text{NO}_2$  which can readily oxidize sulfite species that are formed during the  $\text{SO}_2 + \text{O}_2$  exposure. It is worth mentioning that the similar experiments performed on 8(20)Ba/Al samples (data not shown) revealed qualitatively similar results indicating the suppression of  $\text{NO}_x$  uptake upon sulfur poisoning.

### 3.5. Thermal stability of the adsorbed $\text{NO}_x$ species on the sulfur-poisoned materials

In order to have a better understanding of the influence of  $\text{SO}_2 + \text{O}_2$  treatment on the thermal stability and the desorption properties of the  $\text{NO}_x$  species, TPD experiments were performed. Fig. 8 shows the  $\text{NO}_x$  desorption profiles from the fresh and  $\text{SO}_x$  poisoned  $\gamma\text{-Al}_2\text{O}_3$  and  $\text{TiO}_2$  (anatase) benchmark samples. For clarity, only the  $m/z = 30$ ,  $m/z = 32$  and  $m/z = 46$  desorption channels are shown. For the fresh alumina surface, two major  $\text{NO}$  and  $\text{NO}_2$  desorption features are observed, that is in good agreement with the literature data [20,79]. The first  $\text{NO}_x$  desorption feature at  $387\text{ K}$  is associated with the desorption of monodentate nitrates and weakly bound  $\text{N}_2\text{O}_3$  and/or  $\text{NO}^+$  species which desorb in the form of  $\text{NO}_2$  and  $\text{NO}$  (almost without  $\text{O}_2$ ). The second major desorption band has its maximum at  $625\text{ K}$  and is associated with the desorption/decomposition of bridged and bidentate nitrates which yield a greater  $\text{NO}_2$  desorption signal along with  $\text{NO}$  and  $\text{O}_2$  [20,79].

The  $\text{SO}_2$ -poisoning of the alumina surface has a strong influence on the  $\text{NO}_x$  desorption features. As it is seen in Fig. 8b, sulfur poisoning alters both the type and the quantity of adsorbed  $\text{NO}_x$



**Fig. 6.** FTIR spectra monitored after  $\text{NO}_2$  adsorption at 323 K on fresh (black spectra) and poisoned (red spectra) (a)  $\gamma\text{-Al}_2\text{O}_3$ , (b)  $\text{TiO}_2$  (anatase), (c) Ti/Al(P1), (d) Ti/Al(P2) samples. Poisoning was performed by exposing the samples to 0.6 Torr  $\text{SO}_2(\text{g}) + \text{O}_2(\text{g})$  ( $\text{SO}_2:\text{O}_2 = 1:10$ ) at 323 K, followed by heating in the gaseous mixture at 473 K for 30 min and a final evacuation at 323 K ( $P_{\text{reactor}} < 1 \times 10^{-3}$  Torr).  $\text{NO}_x$  uptake was performed by exposing the samples to 8 Torr of  $\text{NO}_2(\text{g})$  at 323 K for 20 min, followed by evacuation to  $< 1 \times 10^{-3}$  Torr. All spectra were acquired in vacuum at 323 K. (For interpretation of the references to color in this figure legend, the reader is referred to the web version of this article.)

species. For the poisoned sample, the major feature around 380 K (associated with the monodentate nitrates or weakly bound  $\text{N}_2\text{O}_3$  desorption) appears to a larger extent than desorption of bidentate/bridged nitrate at 675 K. This finding is also consistent with the FTIR results obtained for  $\text{NO}_2$  adsorption on the sulfated  $\gamma\text{-Al}_2\text{O}_3$  surface, yielding the band corresponding to adsorbed  $\text{NO}^+/\text{N}_2\text{O}_3$  species at  $1958\text{ cm}^{-1}$  (Fig. 6a). Relatively lower intensity of the  $1958\text{ cm}^{-1}$  band (Fig. 5a) in comparison to the other  $\text{NO}_x$  bands could be associated with its low IR absorption cross-section. Thus,  $\text{SO}_x$  species seem to compete with the nitrate species for surface adsorption sites. Furthermore, in the presence of  $\text{SO}_x$  species,

strongly adsorbed nitrates are partially consumed and converted into weakly bound  $\text{N}_2\text{O}_3$  (reactions (2) and (7)) or  $\text{NO}^+$  (reaction (3)) while some of the sulfites and chemisorbed  $\text{SO}_2$  species are converted into sulfates through reactions similar to the ones proposed above (pathway II).

Fig. 8c and d shows the TPD profiles for  $\text{NO}_x$  desorption from fresh and  $\text{SO}_x$  poisoned  $\text{TiO}_2$  (anatase) samples. Fresh  $\text{TiO}_2$  sample presents a weak shoulder at 455 K and two broad features located at 610 and 900 K in NO desorption curve. In the light of the former studies [74–77] the shoulder at 455 K can be related to molecularly bound  $\text{NO}_2$  species and monodentate nitrates. The band at

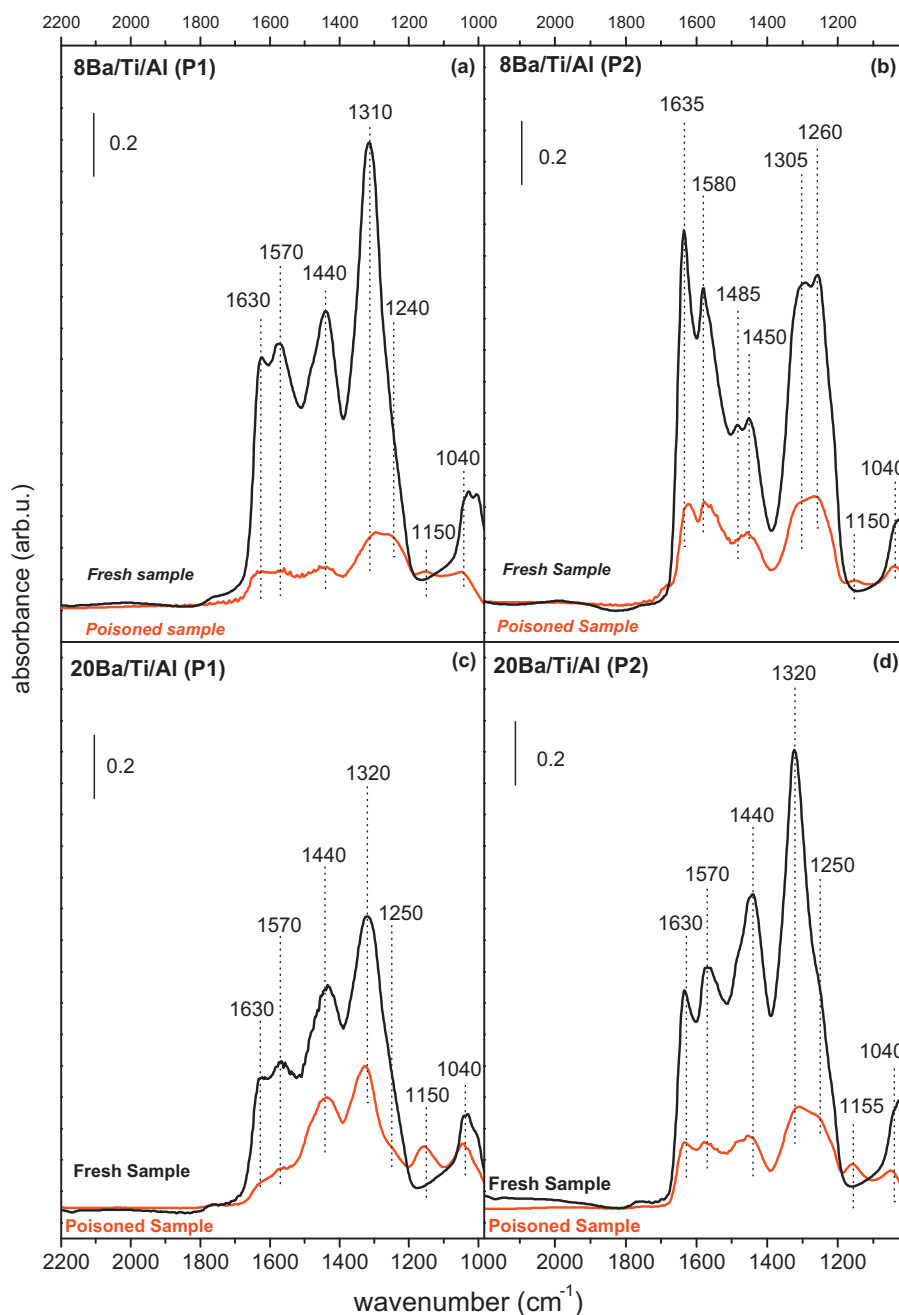


**Fig. 7.** FTIR spectra monitored after  $\text{NO}_2$  adsorption at 323 K on fresh (black spectra) and poisoned (red spectra) (a) 8Ba/Ti/Al(P1), (b) 8Ba/Ti/Al(P2), (c) 20Ba/Ti/Al(P1), (d) 20Ba/Ti/Al(P2) samples. Poisoning was performed by exposing to 0.6 Torr  $\text{SO}_2(\text{g}) + \text{O}_2(\text{g})$  ( $\text{SO}_2:\text{O}_2 = 1:10$ ) at 323 K, followed by heating in the gaseous mixture at 473 K for 30 min and a final evacuation at 323 K ( $P_{\text{reactor}} < 1 \times 10^{-3}$  Torr).  $\text{NO}_x$  uptake was performed by exposing the samples to 8 Torr of  $\text{NO}_2(\text{g})$  at 323 K for 20 min, followed by evacuation. All spectra were acquired in vacuum at 323 K. (For interpretation of the references to color in this figure legend, the reader is referred to the web version of this article.)

610 K is attributed to the desorption/decomposition of the bridged and bidentate nitrates. The high temperature desorption feature at 900 K can be attributed to the desorption of strongly bound nitrates. It is known [23] that phase transition from bulk anatase to bulk rutile starts at  $T > 800$  K. Therefore the strong  $\text{NO}_x$  desorption signal at 900 K in Fig. 8c could be associated with the drastic decrease in the surface area of  $\text{TiO}_2$  as a result of the phase transition from anatase to the rutile phase. Note that during the activation of the fresh and poisoned anatase surfaces before the TPD experiments,  $\text{TiO}_2$  samples were not exposed to temperatures higher than 623 K in order to preserve the anatase phase purity thus, the activation was performed via  $\text{O}_2(\text{g})$  rather than  $\text{NO}_2(\text{g})$ .

The poisoned  $\text{TiO}_2$  sample shows an additional minor desorption feature at 345 K (Fig. 8d). We attribute this feature to the desorption of weakly adsorbed  $\text{N}_2\text{O}_3/\text{NO}^+$  (desorption occurs mainly in the form of  $\text{NO} + \text{NO}_2$ ). The desorption feature at 450 K is associated with weakly adsorbed molecular species and/or with monodentate nitrates. TPD profile of the poisoned  $\text{TiO}_2$  sample (Fig. 8d) reveals a decrease in the 450 K desorption signal with respect to that of the fresh sample (Fig. 8c) in agreement with the FTIR data (Fig. 6b) indicating a suppression of the monodentate nitrate signals at 1550 and 1282  $\text{cm}^{-1}$  upon poisoning. The main desorption band for the poisoned  $\text{TiO}_2$  sample occurs at 615 K indicating that on the poisoned anatase,  $\text{NO}_2$  adsorbs predominantly in

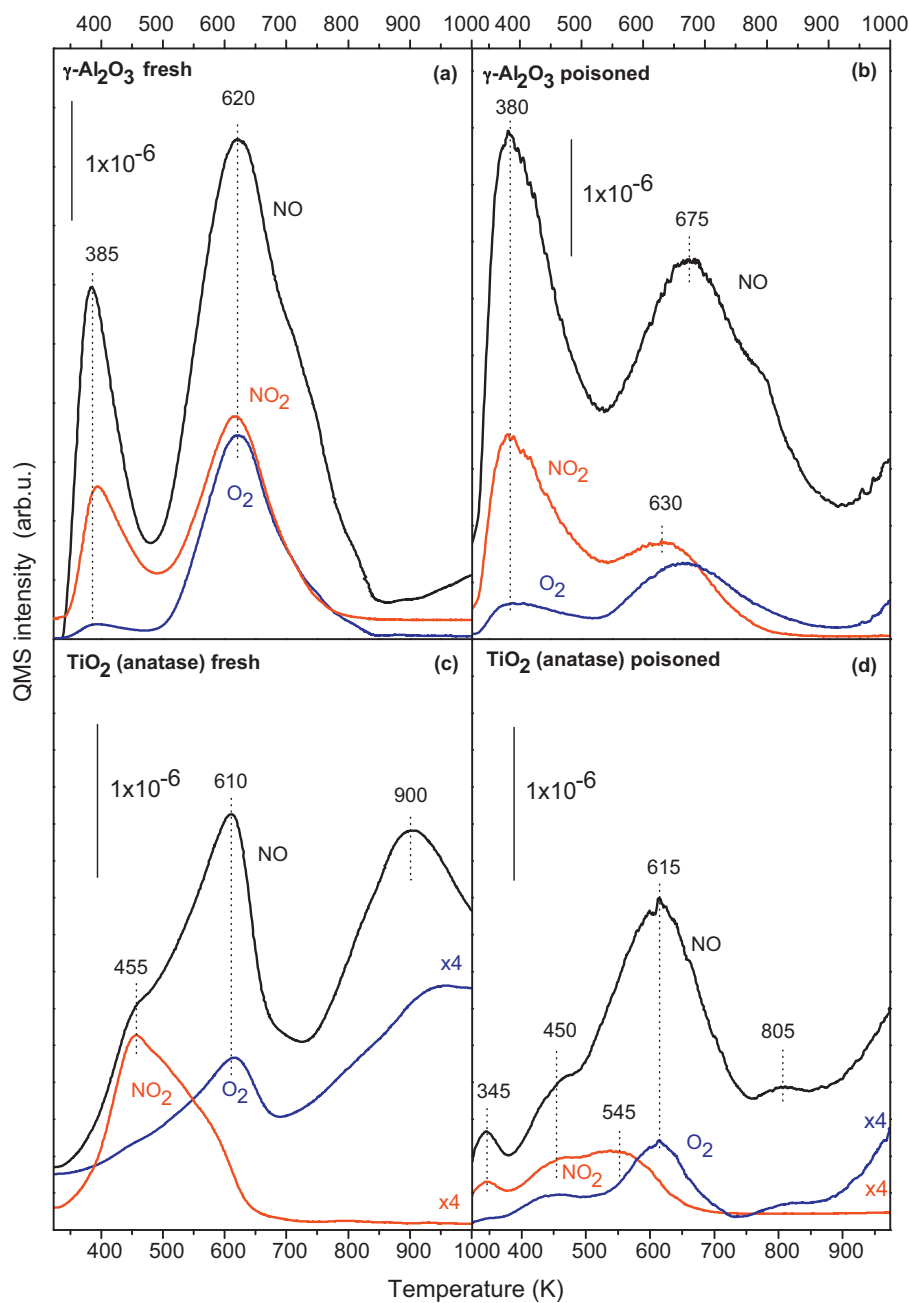


**Fig. 8.** TPD profiles obtained from fresh and poisoned (a and b)  $\gamma\text{-Al}_2\text{O}_3$ , (c and d)  $\text{TiO}_2$  (anatase) samples after saturation with 8 Torr  $\text{NO}_2(\text{g})$  at 323 K for 20 min. Black, blue and red curves correspond to  $m/z=30$  (NO),  $m/z=32$  ( $\text{O}_2$ ) and  $m/z=46$  ( $\text{NO}_2$ ) signals, respectively. Poisoning was performed by exposing the samples to 0.6 Torr  $\text{SO}_2(\text{g}) + \text{O}_2(\text{g})$  ( $\text{SO}_2:\text{O}_2 = 1:10$ ) at 323 K, followed by heating in this gaseous mixture at 473 K for 30 min and a final evacuation at 323 K. (For interpretation of the references to color in this figure legend, the reader is referred to the web version of this article.)

the form of bridged/bidentate nitrates. An important aspect of the poisoned anatase TPD profile is the lack of a strong desorption signal at  $T > 800$  K suggesting the blocking of the strong  $\text{NO}_x$  adsorption sites by sulfates.

Fig. 9a and b presents the  $\text{NO}_x$  desorption profiles of fresh and poisoned Ti/Al(P1) samples. Taking into consideration the surface morphology of the fresh Ti/Al(P1) sample, which is composed of relatively ordered and well-crystallized  $\text{Al}_2\text{O}_3$  and  $\text{TiO}_2$  domains, the low temperature peaks of NO and  $\text{NO}_2$  desorption at 355 and 395 K can be attributed to desorption of weakly adsorbed  $\text{N}_2\text{O}_3$  ( $\text{NO}^+$ ) and/or monodentate nitrates on the alumina domains. Desorption of bridged and bidentate nitrates occurs in the form of  $\text{NO}_2 + \text{O}_2$  at 625 K while the 780 K desorption signal is observed in the form of  $\text{NO} + \text{O}_2$ . The desorption signal at 625 K in Fig. 9a may originate

from both alumina and titania domains of Ti/Al(P1) since similar features exist in the TPD profiles of pure  $\text{TiO}_2$  and  $\text{Al}_2\text{O}_3$  samples (Fig. 8a and c). On the other hand, the major desorption signal in Fig. 9a appearing at 780 K with a shoulder at 870 K has a significantly higher desorption temperature than any of the pure  $\text{Al}_2\text{O}_3$  desorption features. Thus, the 870 K feature in Fig. 9a can be attributed to the decomposition of strongly bound nitrates on the  $\text{TiO}_2$  domains or on the peripheral adsorption sites which are located at the interface between  $\text{TiO}_2$  and  $\text{Al}_2\text{O}_3$  domains. It is important to mention that the origin of this desorption feature is probably quite different than the 900 K desorption signal in Fig. 8c which is observed for pure anatase. Our previous [23,37] XRD, Raman spectroscopy and BET analysis results indicate that on Ti/Al(P1, P2) surfaces, anatase to rutile and  $\gamma\text{-Al}_2\text{O}_3 \rightarrow \alpha\text{-Al}_2\text{O}_3$  phase transformation phenomena

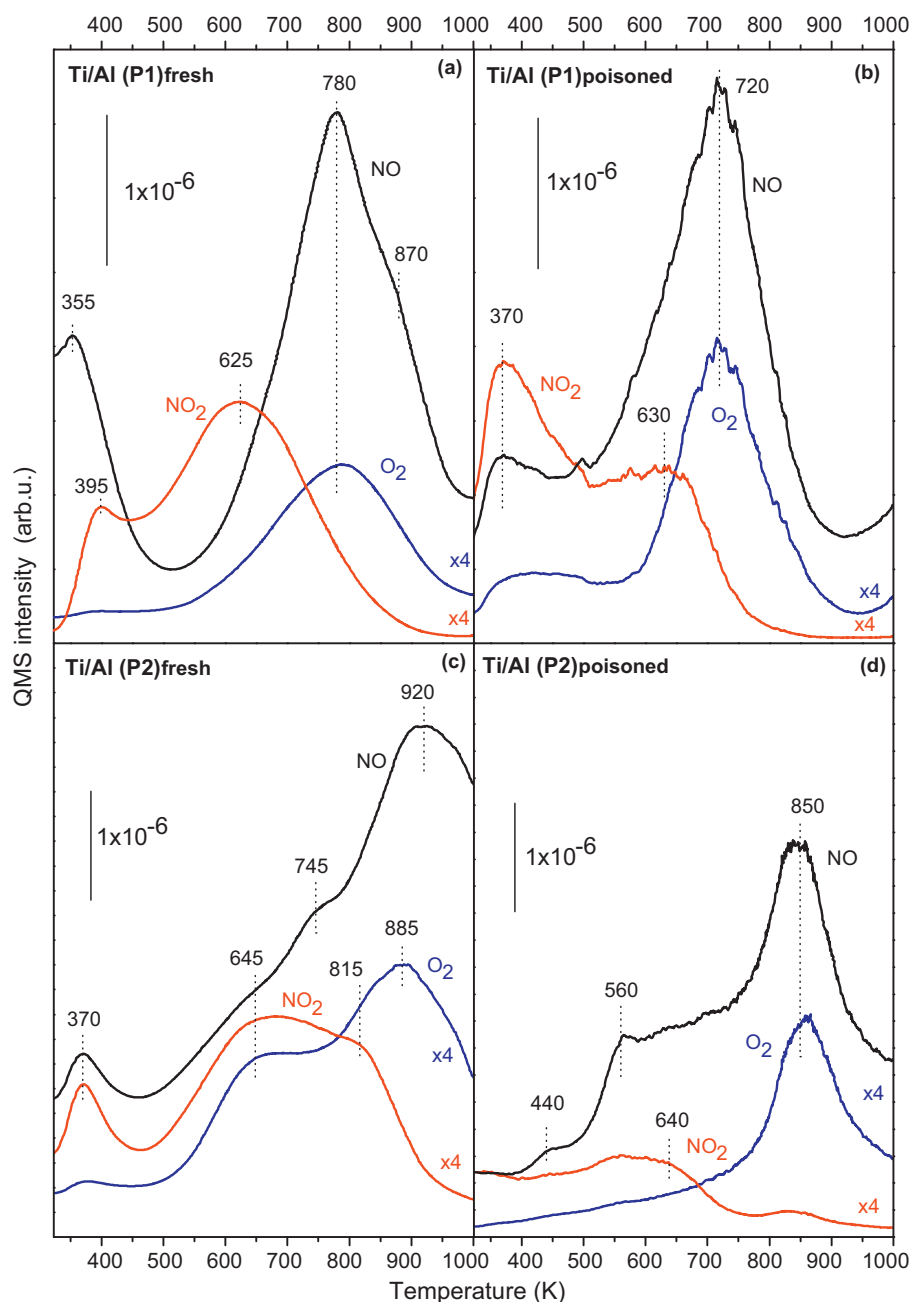


**Fig. 9.** TPD profiles obtained from fresh and poisoned (a and b) Ti/Al(P1), (c and d) Ti/Al(P2) samples saturated with 8 Torr  $\text{NO}_2(\text{g})$  at 323 K for 20 min. Black, blue and red curves correspond to  $m/z=30$  (NO),  $m/z=32$  ( $\text{O}_2$ ) and  $m/z=46$  ( $\text{NO}_2$ ) signals, respectively. Poisoning was performed by exposing the samples to 0.6 Torr  $\text{SO}_2(\text{g}) + \text{O}_2(\text{g})$  ( $\text{SO}_2:\text{O}_2 = 1:10$ ) at 323 K, followed by heating in this gaseous mixture at 473 K for 30 min and a final evacuation at 323 K. (For interpretation of the references to color in this figure legend, the reader is referred to the web version of this article.)

occur only at temperatures higher than 1073 K. Accordingly, only a moderate decrease in the specific surface area values are observed at  $T \leq 900$  K. Thus, it is unlikely that the 870 K feature in Fig. 9a is due to anatase to rutile or  $\gamma\text{-Al}_2\text{O}_3 \rightarrow \alpha\text{-Al}_2\text{O}_3$  phase transitions or any other associated drastic attenuation in the surface area of the samples. Another interesting aspect of the TPD data given in Fig. 9 is the relatively low intensity of the  $\text{O}_2$  desorption signals in comparison with that of the NO desorption signals. One possible explanation for this observation is that, during the vacuum annealing and activation of the Ti/Al(P1, P2) samples inside the IR-TPD cell, some of the surface  $\text{TiO}_2$  domains may be partially reduced. These reduced  $\text{TiO}_2$  surface domains containing oxygen defects are healed by the oxygen species that are generated during the decomposition of the nitrate species in the course of the TPD experiments.

After poisoning of the Ti/Al(P1) sample, desorption of the weakly adsorbed  $\text{NO}_x$  species at  $< 400$  K proceeds mainly in the form of  $\text{NO}_2$  (Fig. 9b). One can also see that  $\text{NO}_2$  desorption peak at 625–630 K is significantly diminished. Furthermore, the most prominent  $\text{NO}_x$  desorption feature shifts to a lower temperature by 60 K and is located at 720 K for the poisoned Ti/Al(P1) sample. This is accompanied by the almost complete disappearance of the high temperature NO desorption signal at 870 K. It is clear that the presence of sulfite and sulfate species on the Ti/Al(P1) surface leads to the blocking of the strong  $\text{NO}_x$  binding sites and inhibits the formation of strongly bound nitrates. In addition,  $\text{SO}_x$  accumulation on the surface also destabilizes the nitrate species which are bound to intermediate-strength  $\text{NO}_x$  adsorption sites on Ti/Al(P1).

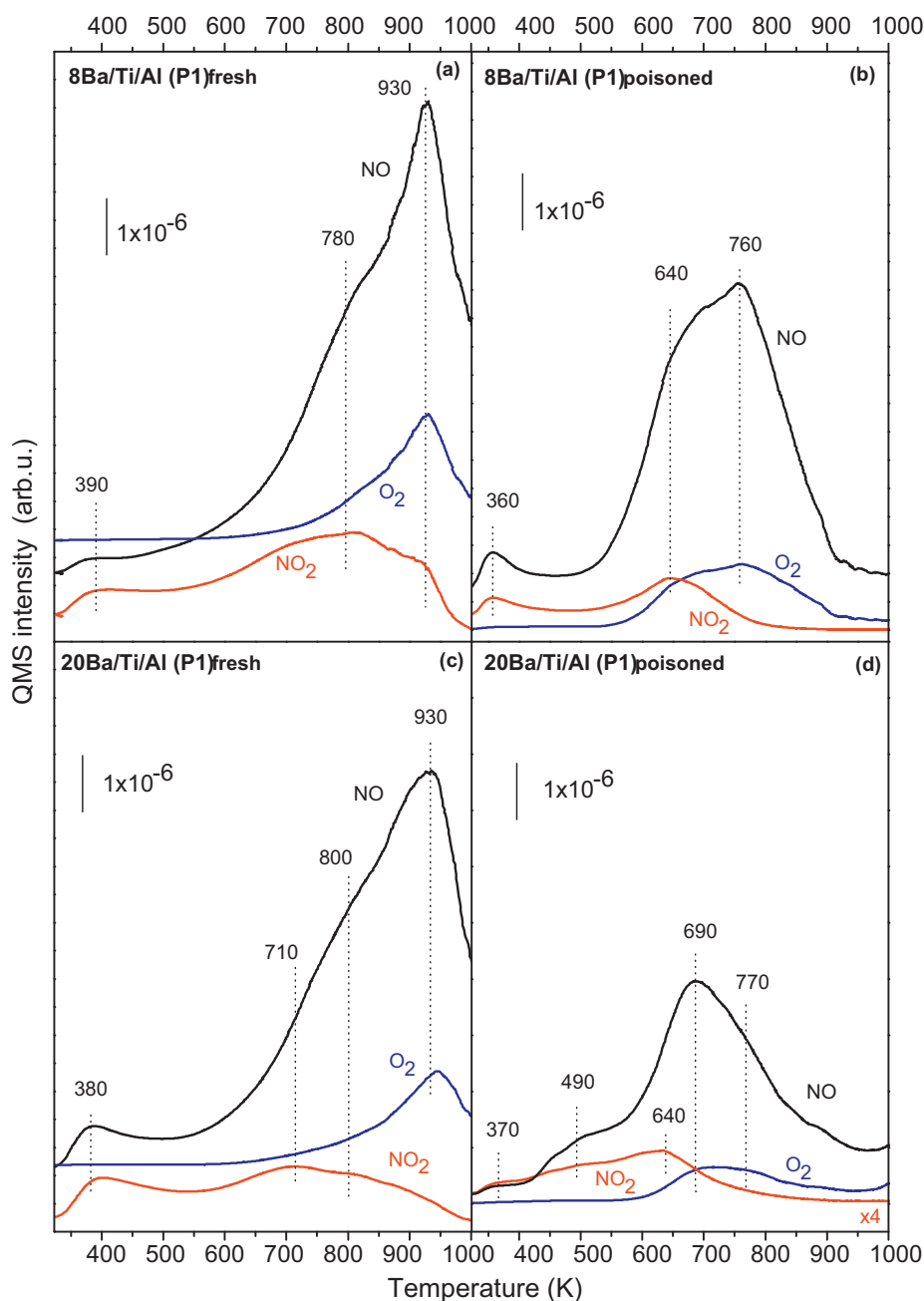


**Fig. 10.** TPD profiles obtained from fresh and poisoned (a and b) 8Ba/Ti/Al(P1), (c and d) 20Ba/Ti/Al(P1) samples saturated with 8 Torr  $\text{NO}_2(\text{g})$  at 323 K for 20 min. Black, blue and red curves correspond to  $m/z=30$  (NO),  $m/z=32$  ( $\text{O}_2$ ) and  $m/z=46$  ( $\text{NO}_2$ ) signals, respectively. Poisoning was performed by exposing the samples to 0.6 Torr  $\text{SO}_2(\text{g}) + \text{O}_2(\text{g})$  ( $\text{SO}_2:\text{O}_2=1:10$ ) at 323 K, followed by heating in this gaseous mixture at 473 K for 30 min and a final evacuation at 323 K. (For interpretation of the references to color in this figure legend, the reader is referred to the web version of this article.)

The TPD profile of fresh Ti/Al(P2) (Fig. 9c) demonstrates minor NO and  $\text{NO}_2$  desorption peaks at 370 K and some broad NO,  $\text{NO}_2$  and  $\text{O}_2$  desorption features that appear between 645–745 K. These features can be attributed to the  $\text{NO}_x$  desorption from  $\text{Al}_2\text{O}_3$  domains [37] of the Ti/Al(P2) surface. This sample also reveals a NO desorption signal at 900–920 K which can be associated with strongly bound bidentate or bridging nitrates adsorbed on the disordered and defective binding sites of the porous  $\text{Ti}_x\text{Al}_y\text{O}_z$  mixed oxide surface.

After poisoning (Fig. 9d) the Ti/Al(P2) sample, the presence of sulfates inhibits the adsorption of  $\text{NO}_x$  species particularly on the weak ( $T < 550$  K) and strong ( $T > 870$  K)  $\text{NO}_x$  binding sites, while influencing the intermediate-strength  $\text{NO}_x$  binding

sites ( $550 \text{ K} < T < 870 \text{ K}$ ) to a lesser extent. Thus, formation of weakly bound ( $\text{N}_2\text{O}_3/\text{NO}^+/\text{NO}_2$ ) as well as strongly bound bidentate/bridging nitrates are significantly suppressed after poisoning. Along these lines, the main NO and  $\text{NO}_2$  desorption features are also shifted to lower temperatures after  $\text{SO}_x$  poisoning indicating the destabilization of the adsorbed nitrates.

Similar TPD experiments were also performed on Ba containing Ba/Ti/Al systems and the representative data corresponding to some of these experiments are presented below. The  $\text{NO}_x$  desorption features from the fresh 8Ba/Ti/Al(P1) sample upon  $\text{NO}_2$  adsorption at 323 K are presented in Fig. 10a. The dominant feature at 930 K is associated with the decomposition of the bulk Ba-nitrates on the large BaO clusters which are located on the

agglomerated TiO<sub>2</sub> particles [23]. The low-temperature features are attributed to the convolution of signals originating from the decomposition of nitrates on large TiO<sub>2</sub> crystallites (780 K) and the decomposition of the surface (bidentate) nitrates on Ba-domains (650–700 K) [23].

The poisoning of 8Ba/Ti/Al(P1) sample with SO<sub>x</sub> at 323 K, prior to the NO<sub>2</sub> adsorption increases the desorption signal of the weakly adsorbed species (Fig. 10b) as observed in the case of the corresponding support material Ti/Al(P1). The prominent NO<sub>x</sub> desorption band observed for the poisoned sample is located at 760 K, with a shoulder at 640 K. The high temperature desorption feature at 930 K is not detected for the poisoned 8Ba/Ti/Al(P1) sample, suggesting the interaction of the SO<sub>x</sub> species with the larger BaO clusters and suppression of the formation of thermally stable bulk nitrate species by blocking the surface sites and limiting the diffusion of nitrates into the subsurface of the BaO clusters. Unlike the fresh sample, poisoned sample yields more pronounced NO<sub>x</sub> desorption features at ~640 K associated with surface BaO and TiO<sub>2</sub> sites rather than bulk BaO. Furthermore, it is worth mentioning that the desorption/decomposition of the stored NO<sub>x</sub> is completed at ca. 900 K for the poisoned 8 Ba/Ti/Al(P1) sample which clearly emphasizes the destabilization effect of the sulfates on the stored nitrate species.

TPD data given in Fig. 10c and d for the 20Ba/Ti/Al(P1) also demonstrate the suppression of the high-temperature desorption signal located at 900–950 K after sulfur poisoning. Concomitantly, medium-temperature NO desorption signal at 600–800 K which is associated with nitrates on well-dispersed titania domains as well as nitrates on alumina sites is also suppressed to a certain extent. Suppression of the bulk Ba(NO<sub>3</sub>)<sub>2</sub> formation upon sulfur poisoning was also observed in similar TPD experiments (data not shown) performed with 8(20)Ba/Ti/Al(P2) samples.

### 3.6. Thermal stability of the adsorbed SO<sub>x</sub> species

During TPD experiments given in section 3.5, which were performed after the saturation of SO<sub>x</sub>-poisoned surfaces with NO<sub>2</sub>, desorption of SO<sub>2</sub> (*m/z* = 64) was also monitored in a parallel fashion to the NO<sub>x</sub> desorption channels. It is worth mentioning that SO<sub>2</sub> was the only significant SO<sub>x</sub> species desorbing from the investigated surfaces in addition to a very minor amount of H<sub>2</sub>S (*m/z* = 34) species whose intensity was at least 20-fold smaller than that of SO<sub>2</sub>. The SO<sub>2</sub> and H<sub>2</sub>S desorption channels of these TPD experiments are presented in Fig. 11.

The general characteristics of the SO<sub>x</sub> desorption from the TiO<sub>2</sub> (anatase) surface (Fig. 11) reveal relatively unstable SO<sub>x</sub> species that desorb at 452 K as a broad peak (due to SO<sub>3</sub><sup>2-</sup> and/or weakly bound molecular SO<sub>2</sub>). At 760 K, an intense SO<sub>2</sub> desorption signal is visible. This drastic SO<sub>2</sub> evolution at a rather low temperature (i.e. 760 K) could be associated with the decomposition of sulfates as a result of the anatase to rutile phase transition and the collapse of the porous anatase structure to form the low-surface area rutile polymorph. For γ-Al<sub>2</sub>O<sub>3</sub>, two major desorption signals are observed in the SO<sub>2</sub> desorption trace. The first desorption maximum appears at 510 K and is probably associated with SO<sub>3</sub><sup>2-</sup> and/or weakly bound molecular SO<sub>2</sub>. The second and the most prominent desorption signal starts to appear at *T* > 900 K and reveals a large desorption signal whose desorption maximum is beyond the ultimate temperature limit (i.e. ca. 1020 K) that can be reached in the current TPD experimental setup. This high temperature SO<sub>2</sub> desorption signal is attributed to the strongly bound surface and/or bulk sulfates on alumina [80].

The SO<sub>2</sub> desorption profile of the poisoned Ti/Al(P1) (Fig. 11) surface appears as two convoluted but distinguishable low temperature features at 480 and 542 K as well as a high temperature feature

which barely starts to appear at 900 K (whose desorption maximum is likely located at *T* ≫ 1020 K). Comparison of the low-temperature bands arising from the Ti/Al(P1) surface with the γ-Al<sub>2</sub>O<sub>3</sub> and TiO<sub>2</sub> reference materials, indicates that the 480 K feature is most likely associated with the desorption from TiO<sub>2</sub> domains, while the 542 K feature is associated with the desorption from Al<sub>2</sub>O<sub>3</sub> domains. In the low temperature region, SO<sub>2</sub> desorption probably takes place from both γ-Al<sub>2</sub>O<sub>3</sub> and TiO<sub>2</sub> domains while the high temperature desorption feature appearing at *T* > 1000 K could be related to the sulfate desorption from the γ-Al<sub>2</sub>O<sub>3</sub> domains or from the TiO<sub>2</sub>–Al<sub>2</sub>O<sub>3</sub> hetero-junction (interface) sites. The most important aspect of the SO<sub>2</sub> desorption signal from the Ti/Al(P1) sample is that the strongly bound sulfate species desorb at a temperature higher than that of the γ-Al<sub>2</sub>O<sub>3</sub> surface. The SO<sub>2</sub> desorption profile of the Ti/Al(P2) sample (Fig. 11d) demonstrates a broad desorption signal within 400–800 K with a maximum at 590 K. This broad peak can be envisioned as a convolution of all of the low-temperature SO<sub>2</sub> desorption features that are observed for TiO<sub>2</sub>, Al<sub>2</sub>O<sub>3</sub> and Ti/Al(P1) which is in line with the poorly defined and the amorphous surface structure of the Ti/Al(P2) samples. It is important to mention that the SO<sub>2</sub> desorption features for Ti/Al(P2) in the intermediate temperature region (400–800 K) appear higher than that of Ti/Al(P1). This observation indicates that the thermal stability of SO<sub>x</sub> species on the Ti/Al(P2) surface is higher than that of Ti/Al(P1). Apparently Ti/Al(P2) sample also presents a high-temperature SO<sub>2</sub> signal which starts to evolve at *T* > 970 K with a desorption maximum located at *T* ≫ 1020 K. Initial take-off for this high-temperature desorption feature also starts at a higher temperature than the corresponding feature for Ti/Al(P1) consistent with the higher stability of SO<sub>x</sub> species on Ti/Al(P2). The SO<sub>x</sub> desorption profiles of all of the Ba-containing samples were rather similar to each other (Fig. 11), presenting a low-temperature SO<sub>2</sub> desorption signal with a broad line shape within 400–700 K. This is followed by a high-temperature SO<sub>2</sub> desorption signal at *T* > 1000 K, which was above the temperature window accessible with the currently used TPD experimental setup. Thus, although the current TPD experiments cannot discriminate the relative thermal stabilities of the strongly bound SO<sub>x</sub> species, FTIR technique can provide valuable insights regarding this point, as described below.

Fig. 12 shows an interesting set of FTIR data demonstrating the thermal regeneration capabilities of the TiO<sub>2</sub>-promoted samples after sulfur poisoning. These series of FTIR spectra were obtained on samples which are initially poisoned with SO<sub>2</sub> + O<sub>2</sub> at 323 K and then successively saturated with NO<sub>2</sub> at 323 K and finally evacuated in vacuum at 1023 K. After the high-temperature evacuation, all of the adsorbed NO<sub>x</sub> species were found to desorb from all of the investigated surfaces. However some of the thermally stable adsorbed SO<sub>x</sub> species still exist on the sample surfaces, even after the thermal regeneration treatment at 1023 K. Considering the data corresponding to the 8Ba/Al and 20Ba/Al conventional benchmark samples in Fig. 12, it is apparent that these conventional NO<sub>x</sub> storage materials still possess a significant amount of stable surface aluminum sulfates (1360 and 1125 cm<sup>-1</sup>) and bulk BaSO<sub>4</sub> (1258 and 1160 cm<sup>-1</sup>) even after thermal regeneration treatment at 1023 K. In other words, the effect of sulfur poisoning is relatively severe and irreversible on conventional TiO<sub>2</sub>-free materials, leading to extremely stable SO<sub>x</sub> species that cannot be readily removed even after evacuation at elevated temperatures.

On the other hand, TiO<sub>2</sub>-promoted samples given in Fig. 12 show a much better thermal regeneration behavior, revealing significantly smaller intensities corresponding to the SO<sub>x</sub> vibrational features after evacuation at 1023 K. This is particularly valid for 8Ba/Ti/Al(P1, P2) and 20Ba/Ti/Al(P1) samples. Combining these results with the relative total SO<sub>x</sub> uptake data presented in

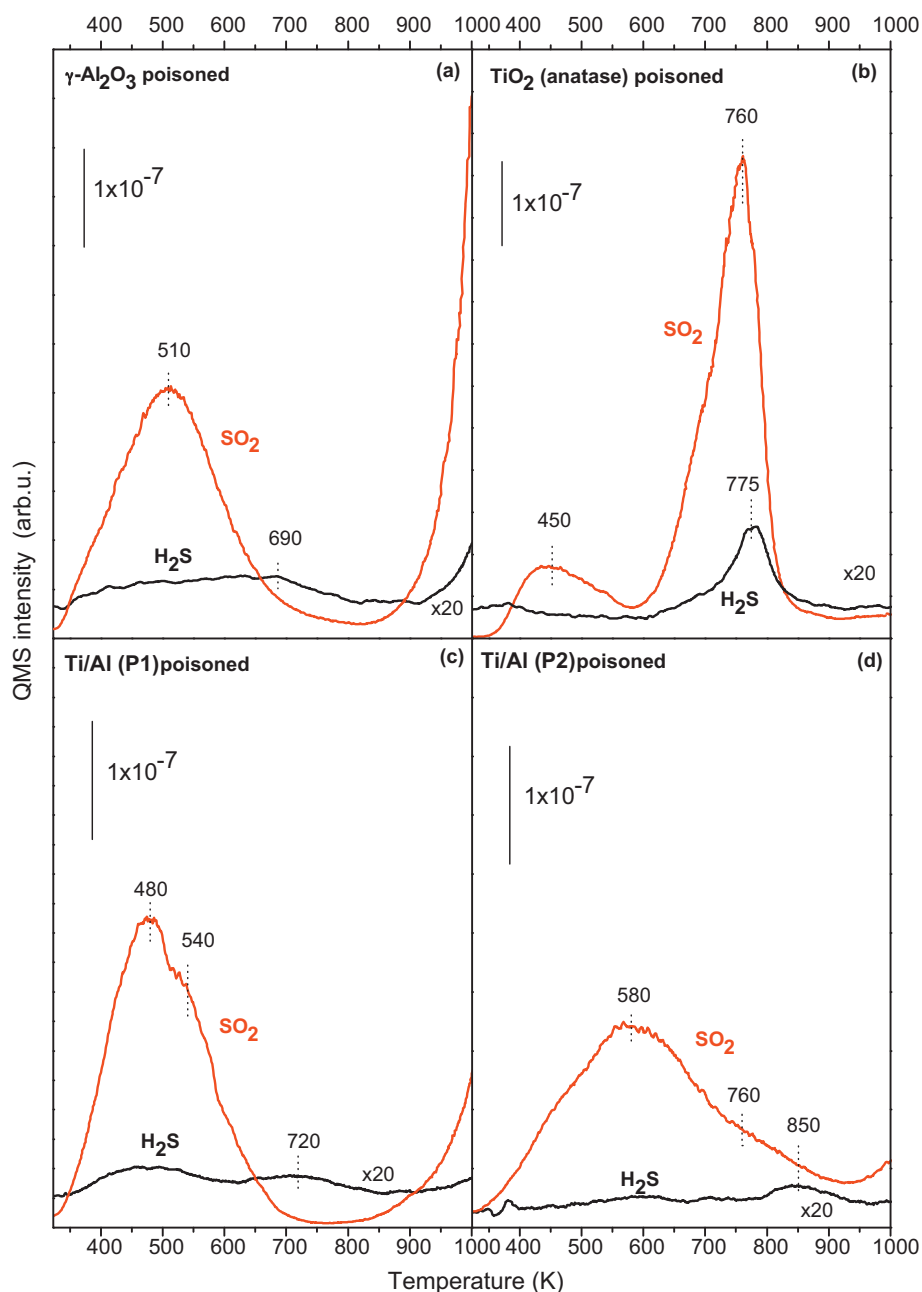


**Fig. 11.** SO<sub>2</sub> desorption profiles in TPD experiments for  $\gamma$ -Al<sub>2</sub>O<sub>3</sub>, TiO<sub>2</sub>, Ti/Al(P1 and P2), samples which were initially poisoned with 0.6 Torr SO<sub>2</sub>(g) + O<sub>2</sub>(g) (SO<sub>2</sub>:O<sub>2</sub> = 1:10) at 473 K for 30 min and then evacuated and successively treated with 8 Torr NO<sub>2</sub>(g) at 323 K for 20 min (see text for details).

Fig. 5, it is clear that 8Ba/Ti/Al(P1, P2) and 20Ba/Ti/Al(P1) samples not only accumulate a smaller amount of SO<sub>x</sub> species than the conventional 8(20)Ba/Al materials upon sulfur poisoning, but they also significantly destabilize the adsorbed SO<sub>x</sub> species and facilitate their effective thermal regeneration/removal via simple annealing at 1023 K without an additional reducing agent such as CO, H<sub>2</sub> or hydrocarbons. It is also important to mention that the thermal regeneration temperature that is used in the current work (i.e. 1023 K) is close to temperatures used in such thermal SO<sub>x</sub> removal treatments in realistic exhaust emission systems (e.g. 750 °C). It is worth mentioning that the current findings are in very good agreement with the recent transient response measurement (TRM) studies [81] performed on nano-structured Pt/BaO/TiO<sub>2</sub>/Al<sub>2</sub>O<sub>3</sub> NSR catalysts reporting that TiO<sub>2</sub> promotion

facilitates both the SO<sub>x</sub> removal and the catalyst regeneration under operational conditions while enhancing the total NO<sub>x</sub> storage capacity. As can be seen in Fig. 5, 20Ba/Ti/Al(P2) sample is the only sample which was found to store a larger amount of SO<sub>x</sub> in comparison to its TiO<sub>2</sub>-free counterpart (i.e. 20Ba/Al). However the thermal regeneration of this sample (Fig. 12b) reveals a slightly better SO<sub>x</sub> removal behavior than the 20Ba/Al case, indicating the positive influence of TiO<sub>2</sub>-promotion on the destabilization of the SO<sub>x</sub> species. It is worth mentioning that we have also attempted to quantitatively analyze the remaining amount of sulfur species after the thermal regeneration step via XPS and EDX. However the sulfur signals in XPS and EDX after the regeneration step were below the analytical detection limits for all samples.

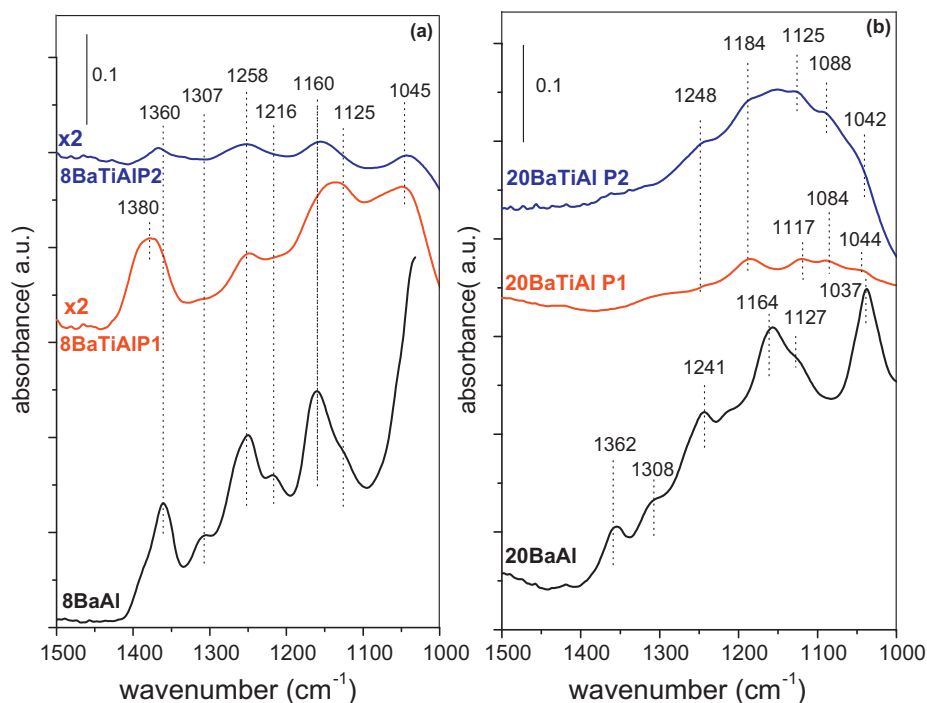


**Fig. 12.** FTIR spectra demonstrating the thermal regeneration capabilities of (a) 8Ba/Al, 8Ba/Ti/Al(P1), 8Ba/Ti/Al(P2) and (b) 20Ba/Al, 20Ba/Ti/Al(P1), 20Ba/Ti/Al(P2) samples after sulfur poisoning. Spectra were obtained at 323 K in vacuum after initial sulfur poisoning with 0.6 Torr  $\text{SO}_2(\text{g}) + \text{O}_2(\text{g})$  ( $\text{SO}_2:\text{O}_2 = 1:10$ ) at 323 K, followed by heating in this gaseous mixture at 473 K for 30 min and a subsequent evacuation at 323 K; followed by 8 Torr  $\text{NO}_2(\text{g})$  adsorption at 323 K for 20 min and a final evacuation step in vacuum at 1023 K.

#### 4. Conclusions

In the current work, we have investigated the structural properties and chemical behavior of  $\text{TiO}_2$ -promoted binary and ternary mixed oxide systems that are particularly relevant to NSR catalytic applications. A systematic approach was followed in which the structural and chemical behavior of the Ti/Al(P1, P2) binary oxide support materials were initially analyzed in a comparative fashion with simple conventional support materials such as  $\gamma\text{-Al}_2\text{O}_3$  and  $\text{TiO}_2$  (anatase). In the light of these initial studies, more complex 8(20)Ba/Ti/Al(P1, P2) ternary oxide  $\text{NO}_x$  storage materials were investigated. Some of the important findings of the current studies can be summarized as follows:

- Surface structure and the morphology of the  $\text{TiO}_2\text{-Al}_2\text{O}_3$  mixed oxide systems strongly depend on the synthesis protocols. Ti/Al(P1) system is comprised of relatively ordered and inhomogeneously distributed  $\text{TiO}_2$  (anatase) crystallites on  $\gamma\text{-Al}_2\text{O}_3$  domains while Ti/Al(P2) system contains an amorphous and a highly porous  $\text{Ti}_x\text{Al}_y\text{O}_z$  structure.
- $\text{SO}_x$  adsorption on all of the investigated samples leads to a decrease in the  $\text{NO}_x$  storage capacity due to the blocking of the  $\text{NO}_x$  adsorption sites by sulfite and sulfate species.
- Ti/Al(P1, P2) systems present a higher  $\text{SO}_x$  storage capacity (per unit sample weight) and a higher thermal stability for the adsorbed  $\text{SO}_x$  species than that of both  $\gamma\text{-Al}_2\text{O}_3$  and  $\text{TiO}_2$  (anatase) surfaces, while Ti/Al(P2) system demonstrates higher affinity towards  $\text{SO}_x$  than Ti/Al(P1) system. This can be explained by the relatively higher SSA of the Ti/Al(P1, P2) systems (better dispersion of  $\text{TiO}_2$  domains on  $\gamma\text{-Al}_2\text{O}_3$  with respect to bulk anatase) as well as the decrease in the total number of Lewis acid sites and the presence of new adsorption sites due to  $\text{TiO}_2$  promotion.
- Typically,  $\text{TiO}_2$ -promoted  $\text{NO}_x$  storage materials (e.g. 8(20)Ba/Ti/Al(P1) and 8Ba/Ti/Al(P2)) accumulate less  $\text{SO}_x$  (per

unit sample weight) than  $\text{TiO}_2$ -free conventional 8(20)Ba/Al samples under identical poisoning conditions. Furthermore the (P1) samples accumulate less  $\text{SO}_x$  than (P2) samples which can be associated with both lower SSA of the (P1) samples and their different surface morphology.

- $\text{TiO}_2$ -promoted 8(20)Ba/Ti/Al(P1, P2)  $\text{NO}_x$  storage materials were found to exhibit superior thermal regeneration behavior after sulfur poisoning in comparison to conventional 8(20)Ba/Al materials. Adsorbed  $\text{SO}_x$  species were observed to be significantly destabilized upon  $\text{TiO}_2$  promotion and thus corresponding sulfate and sulfite species can readily be removed from the surface by simple annealing in vacuum at 1023 K, in the absence of an additional reducing agent such as  $\text{H}_2$ , CO or hydrocarbons. This behavior can be attributed to well-dispersed BaO units on  $\text{TiO}_2$  domains and the suppression of the formation of bulk  $\text{BaSO}_4$  clusters. These results suggest that  $\text{TiO}_2$ -promotion might be a promising strategy for enhancing the sulfur tolerance of NSR systems which results in not only the suppression of the  $\text{SO}_x$  accumulation on the catalyst surface, but also improvement of the thermal regeneration capability of the sulfur-poisoned catalyst and prevention of irreversible sulfur uptake under operational conditions.

#### Acknowledgement

Authors gratefully acknowledge the financial support from the Scientific and Technical Research Council of Turkey (TUBITAK) (Project Code: 108M379). E.O. also acknowledges support from Turkish Academy of Sciences (TUBA) for the “Outstanding Young Investigator” grant. E.V., V. Z. and V. B. acknowledge RFBR (Russia) #09-03-91225-CT.a and #10-03-00596-a, for financial support. Authors also thank Margarita Kantcheva for fruitful discussions and Erman Bengu for his help with the XPS experiments and TEM data analysis.

## References

- [1] J.S. Hepburn, E. Thanaslu, D.A. Dobson, W.L. Watkins, SAE Technical Paper 962051, 1996.
- [2] W. Bögner, M. Krämer, B. Krutzsch, S. Pischinger, D. Voigtländer, G. Wenninger, F. Wirbeleit, M.S. Brogan, R.J. Brisley, D.E. Webster, Appl. Catal. B 7 (1995) 153.
- [3] M. Machida, K. Yasuoka, K. Eguchi, H. Arai, J. Chem. Soc., Chem. Commun. 17 (1990) 1165.
- [4] E. Fridell, M. Skoglundh, S. Johansson, B. Westerberg, A. Torncrona, G. Smedler, Stud. Surf. Sci. Catal. 116 (1998) 537.
- [5] H. Mahzoul, J.F. Brillhac, P. Gilot, Appl. Catal. B 20 (1999) 47.
- [6] E. Fridell, M. Skoglundh, B. Westerberg, S. Johansson, G. Smedler, J. Catal. 183 (1999) 196.
- [7] A. Piéplu, O. Saur, J.-C. Lavalleya, O. Legendreb, C. Nédez, Catal. Rev. 40 (4) (1998) 409.
- [8] W.S. Epling, L.E. Campbell, A. Yezerets, N.W. Currier, J.E. Parks, Catal. Rev. 46 (2004) 163.
- [9] S. Roy, A. Baiker, Chem. Rev. 109 (2009) 4054.
- [10] A. Snis, H. Miettinen, J. Phys. Chem. B 102 (1998) 2555.
- [11] F. Rohr, S.D. Peter, E. Lox, M. Kogel, A. Sassi, L. Juste, C. Rigaudeau, G. Belot, P. Gelin, M. Primet, Appl. Catal. B 56 (2005) 201.
- [12] A.Yu. Stakheev, P. Gabriellsson, I. Gekas, N.S. Teleguina, G.O. Bragina, N.N. Tolkachev, G.N. Baeva, Top. Catal. 42 (2007) 143.
- [13] E.C. Corbos, S. Elbouazzaoui, X. Courtois, N. Bion, P. Marecot, D. Duprez, Top. Catal. 42 (2007) 9.
- [14] S. Matsumoto, Y. Ikeda, H. Suzuki, M. Ogai, N. Miyoshi, Appl. Catal. B 25 (2000) 115.
- [15] S. Matsumoto, S. Kazuaki, T. Shinji, I. Yasuo, Catal. Catal. 42 (2000) 65.
- [16] L.J. Gill, P.G. Blakeman, M.V. Twigg, A.P. Walker, Top. Catal. 28 (2004) 1.
- [17] J.-R. Chang, S.L. Chang, T.-B. Lin, J. Catal. 169 (1997) 338.
- [18] D. Uy, K.A. Wiegand, A.E. O'Neill, M.A. Dearth, W.H. Weber, J. Phys. Chem. B 106 (2002) 387.
- [19] X. Wei, X. Liu, M. Deeba, Appl. Catal. B 58 (2005) 41.
- [20] E. Kayhan, S.M. Andonova, G.S. Şentürk, C.C. Chusuei, E. Ozensoy, J. Phys. Chem. C 114 (2010) 357.
- [21] M. Misono, T. Inui, Catal. Today 51 (1999) 369.
- [22] A. Fritz, V. Pitchon, Appl. Catal. B 13 (1997) 1.
- [23] S.M. Andonova, G.S. Şentürk, E. Kayhan, E. Ozensoy, J. Phys. Chem. C 113 (2009) 11014.
- [24] J. Dawody, I. Tonniea, E. Fridell, M. Skoglundh, Top. Catal. 42–43 (2007) 183.
- [25] R.J. Hendershot, W.B. Rogers, C.M. Snively, B.A. Ogunnaike, Lauterbach, J. Catal. Today 98 (2004) 375.
- [26] R.J. Hendershot, W.B. Rogers, C.M. Snively, Lauterbach, J. Appl. Catal. B 70 (2007) 160.
- [27] J.-Y. Luo, M. Meng, Yu-Q. Zha, Ya-N. Xie, T.-D. Hu, J. Zhang, T. Liu, Appl. Catal. B 78 (2008) 38.
- [28] <http://www.metro.tokyo.jp/ENGLISH/TOPICS/2004/ftac300.htm>.
- [29] K. Yamazaki, T. Suzuki, N. Takahashi, K. Yokota, M. Sugiura, Appl. Catal. B 30 (2001) 459.
- [30] P.T. Fanson, M.R. Horton, W.N. Deglass, Lauterbach, Appl. Catal. B 46 (2003) 393.
- [31] H.Y. Huang, R.Q. Long, R.T. Yang, Appl. Catal. B 33 (2001) 127.
- [32] H. Hirata, I. Hachisuka, Y. Ikeda, S. Tsuji, S. Matsumoto, Top. Catal. 16 (17) (2001) 145.
- [33] T. Takahashi, A. Suda, I. Hachisuka, M. Sugiura, H. Sobukawa, H. Shinjoh, Appl. Catal. B 72 (2007) 187.
- [34] J.R. Sohn, S.H. Lee, P.W. Cheon, H.W. Kim, Bull. Korean Chem. Soc. 25 (5) (2004) 657.
- [35] J. Mu, D.D. Perimutte, Ind. Eng. Chem. Process Des. Dev. 20 (1981) 641.
- [36] K. Yamamoto, R. Kikuchi, T. Takeguchi, K. Eguchi, J. Catal. 238 (2006) 449.
- [37] S.M. Andonova, G.S. Şentürk, E. Ozensoy, J. Phys. Chem. C 114 (2010) 17003.
- [38] H. Suzuki, R. Muramoto, N. Takahashi, Toyota Tech. Rev. 46 (1996) 68.
- [39] H. Imagawa, T. Tanaka, N. Takahashi, S. Matsunaga, A. Suda, H. Shinjoh, Appl. Catal., B 86 (2009) 63.
- [40] B.N. Shelimov, N.N. Tolkachev, O.P. Tkachenko, G.N. Baeva, K.V. Klementiev, A.Yu. Stakheev, V.B. Kazansky, J. Photochem. Photobiol. A 195 (2008) 81.
- [41] K. Kawabata, H. Yoshimatsu, K. Fujiwara, T. Yabuki, A. Osaka, Y. Miura, J. Mater. Sci. 34 (1999) 2529.
- [42] N. Macleod, R. Cropley, J.M. Keel, R.M. Lambert, J. Catal. 221 (2004) 20.
- [43] N. Takahashi, A. Suda, I. Hachisuka, M. Sugiura, H. Sobukawa, H. Shinjoh, Appl. Catal. B 72 (2007) 187.
- [44] Y. Liu, M. Meng, X. Zou, X. Li, Y. Zha, Catal. Commun. 10 (2008) 173.
- [45] Y. Liu, M. Meng, X.-G. Li, L.-H. Guo, Y.-Q. Zha, Chem. Eng. Res. Des. 86 (2008) 932.
- [46] I. Hachisuka, H. Hirata, Y. Ikeda, S. Matsumoto, SAE Technical Paper (2000) 2000-01-1196.
- [47] S. Matsumoto, CATTECH 4 (2000) 102.
- [48] S. Matsumoto, Catal. Today 29 (1996) 43.
- [49] E. Ozensoy, C.H.F. Peden, J. Szanyi, J. Catal. 243 (2006) 149.
- [50] E. Ozensoy, C.H.F. Peden, J. Szanyi, J. Phys. Chem. B 110 (2006) 17001.
- [51] E. Ozensoy, C.H.F. Peden, J. Szanyi, J. Phys. Chem. B 110 (2006) 17009.
- [52] E. Emmez, E.I. Vovk, V.I. Bukhtiyarov, E.Ozensoy, J. Phys. Chem. C 115 (2011) 22438.
- [53] E.I. Vovk, E. Emmez, M. Erbudak, V. Bukhtiyarov, E. Ozensoy, J. Phys. Chem. C, in press, doi: 10.1021/jp208269x.
- [54] K. Nakamoto, Infrared Spectra of Inorganic and Coordination Compounds, 2nd ed., Wiley-Interscience, New York, 1960.
- [55] A.A. Davydov, Molecular Spectroscopy of Oxide Catalyst Surfaces, Wiley, Chichester, England, 2003.
- [56] M.B. Mitchell, N. Sheinker, J. Phys. Chem. 100 (1996) 7550.
- [57] H.G. Karge, I.G. Dalla Lana, J. Phys. Chem. 88 (1984) 1538.
- [58] H.C. Yao, H.K. Stepien, H.S. Gandhi, J. Catal. 67 (1981) 231.
- [59] A. Datta, R.G. Cavel, R.W. Tower, Z.M. George, J. Phys. Chem. 89 (1985) 443.
- [60] C.C. Chang, J. Catal. 53 (1978) 374.
- [61] O. Saur, M. Bensitel, A.B.M. Saad, J.C. Lavalley, C.P. Tripp, B.A. Morrow, J. Catal. 99 (1986) 104.
- [62] K.C. Schreiber, Anal. Chem. 21 (1949) 1168.
- [63] N.B. Colthup, J. Opt. Soc. Am. 6 (1950) 40.
- [64] T. Yamaguchi, T. Jin, K. Tanabe, J. Phys. Chem. 90 (1986) 3148.
- [65] F.A. Miller, C.H. Wilkins, Anal.Chem. 24 (1952) 1253.
- [66] C. Sedlmair, K. Seshan, A. Jentys, J.A. Lercher, Catal. Today 75 (2002) 413.
- [67] M. Waqif, P. Bazin, O. Saur, J.C. Lavalley, G. Blanchard, O. Touret, Appl. Catal. B 11 (1997) 193.
- [68] M.Yu. Smirnov, A.V. Kalinkin, A.V. Pashis, A.M. Sorokin, A.S. Noskov, K.C. Kharas, V.I. Bukhtiyarov, J. Phys. Chem. B 109 (2005) 11712.
- [69] M. Waqif, A. Pieplu, O. Saur, J.C. Lavalley, G. Blanchard, Solid State Ionics 95 (1997) 163.
- [70] T. Jin, T. Yamaguchi, K. Tanabe, J. Phys. Chem. 90 (1986) 4194.
- [71] A.M. Turek, I.E. Wachs, J. Phys. Chem. C 96 (1992) 5000.
- [72] E. Ozensoy, D. Herrling, J. Szanyi, Catal. Today 136 (2008) 46.
- [73] T. Venkov, K. Hadjiivanov, D. Klissurski, Phys. Chem. Chem. Phys. 4 (2002) 2443.
- [74] M. Kantcheva, J. Catal. 204 (2001) 479.
- [75] K. Hadjiivanov, V. Bushev, M. Kantcheva, D. Klissurski, Langmuir 10 (1994) 464.
- [76] J.C.S. Wu, Y.-T. Cheng, J. Catal. 237 (2006) 393.
- [77] G. Ramis, G. Busca, V. Lorenzelli, P. Forzatti, Appl. Catal. 64 (1990) 243.
- [78] K. Ito, S. Kakino, K. Ikeue, M. Machida, Appl. Catal. B 74 (2007) 137.
- [79] J. Szanyi, J.H. Kwak, R.J. Chimentao, C.H.F. Peden, J. Phys. Chem. C 111 (2007) 2661.
- [80] Q. Wu, H. Gao, H. He, J. Phys. Chem. B 110 (2006) 8320.
- [81] I.S. Pieta, W.S. Epling, M. Garcia-Dieguez, J.Y. Luo, M.A. Larrubia, M.C. Herrera, L.J. Alemany, Catal. Today 175 (2011) 55.